Remaining porosity and permeability of compacted crushed rock salt backfill in a HLW repository

Final Report

DBE TECHNOLOGY contribution

Verantwortung für Generationen
Responsibility for Generations
DBE TECHNOLOGY GmbH

Remaining Porosity and Permeability of Compacted Crushed Rock Salt Backfill in a HLW Repository

Final Report

DBE TECHNOLOGY contribution

Jobmann, M., Müller, C., Schirmer, S.

DBE TECHNOLOGY GmbH
Eschenstraße 55
D-31224 Peine

November 2015

The research work that is the basis of this report was funded by the German Federal Ministry for Economic Affairs and Energy (BMWi = Bundesministerium für Wirtschaft und Energie) represented by the Karlsruher Project Management Agency (Karlsruher Institute of Technology, KIT), under contract no. FKZ 02E 10730. The authors alone, however, are responsible for the contents of this study.

Table of contents

1 Introduction

The safe containment of radioactive waste is to be ensured by the geotechnical barriers in combination with the containment-providing rock zone (CRZ). The latter is a key element of the recently developed concept of demonstrating the integrity of the geologic barrier (Krone et al., 2013). As stipulated in the safety requirements of the regulating body the CRZ has to have strong barrier properties, and evidence needs to be provided that it retains its integrity throughout the reference period (BMU, 2010).

The underground openings excavated in the rock salt will close over time due to the creep properties of the rock salt. This process causes deformations in the surrounding rock salt, which leads to a change in stress state in the virgin rock and may impair the integrity of the containment-providing rock zone. In order to limit the effects of these processes, all underground openings will be backfilled with crushed salt. Immediately after backfilling, the crushed salt will have an initial porosity of approx. 35%, which – over time – will be reduced to very low values due to the creep properties of the rock salt. The supporting pressure that builds up in the crushed salt with increasing compaction slows down the creeping of the salt. Major influencing factors are the temperature (with higher temperatures accelerating the salt creeping) and the moisture of the salt, which – due to the related decrease in the resistance of the crushed salt – facilitates its compaction. The phenomenology of these processes and dependencies is understood to a wide extent. This project investigated the duration until compaction is completed and when and under what circumstances the crushed salt will have the sealing properties necessary to ensure safe containment.

Thermo-hydro-mechanical (THM) processes play a crucial role in determining whether solutions which might enter the mine could reach the radioactive waste. This includes changes in material behaviour due to a partial or complete filling of the pore spaces with solution. In this context, the porosity range of < 3% has special significance. The relevant processes influencing the hydraulic parameters of the crushed salt backfill are still not described in sufficient detail. For the compaction of dry crushed salt, various theoretical constitutive approaches have been developed (Spiers et al., 1989, Hein, 1991, Zhang et al., 1993,, Heemann, 2004) and verified within the scope of the BAMBUS project (Bechthold, 2004) where the porosity range $10\%<\Phi<35\%$ has been calibrated.

The contribution of DBE TECHNOLOGY GmbH to the project consisted mainly of microstructural investigations and by applying discrete element computer codes to evaluate their applicability to simulate compaction processes. This work is described in this report.

2 Microstructural Investigations

2.1 Thin Section Analyses

BGR provided samples from compaction studies for initial investigations on microstructures (Tab. 2.1). The samples have different compaction degrees and, thus, different porosities and were compacted both in dry and in moist condition. The individual samples were evacuated in a desiccator and then soaked with a blue resin with very low viscosity. This is to make visual remaining pore spaces at different compaction degrees and after different compaction methods have been used, as these pore spaces could transport fluids. After adequate time had passed and the resin had hardened, thin sections of each sample were prepared. Subsequently, the thin sections were photographed under a microscope.

Photographic logging was carried out in two steps. After the complete thin section had been recorded, selected areas were photographed with a significantly higher resolution in order to be able to carry out detailed analyses. In a second step, the samples soaked with resin were cut open and the cut surfaces were coated with a red resin and polished. This makes pore spaces visible that have been opened by the cut and have not been penetrated by the blue resin. It cannot be excluded that these pores maybe penetrated by gas, but it is assumed that these pores are mainly dead pores that – although they contribute to the total porosity – are not involved in water or brine migration. The images have been analysed and described.

Tab. 2.1: List of samples provided by BGR

Identifier	Material	Size [cm]	Compaction rate [mm/h]	T [°C]	Test duration [d]	Void ratio
Oedo-047/5	z2Hs	7.0x3.7x1.4	0.36 – 0.00036	200	78	0.006
Oedo-051/8	z2Hs	7.8x5.2x1.6	3.6 – 0.36	100	6	0.063
Oedo-051/9	z2Hs	7.8x5.2x1.6	3.6 – 0.36	100	6	0.063
Oedo-056/5	z2Hs+ 1.2% solution	7.0x3.7x1.4	0.36 – 0.00036	~30	112	0.031
Oedo-102/1	z2Hs+ air moisture	6.0x5.0x1.8	0.36 – 0.00036	~33	134	0.046
Oedo-102/2	z2Hs+ air moisture	6.0x5.0x1.8	0.36 – 0.00036	~33	134	0.046
D-A-025/2	Z2Hs (seeped)	6.0x2.0x3.0	n. s.	~30	n. s.	n. s.

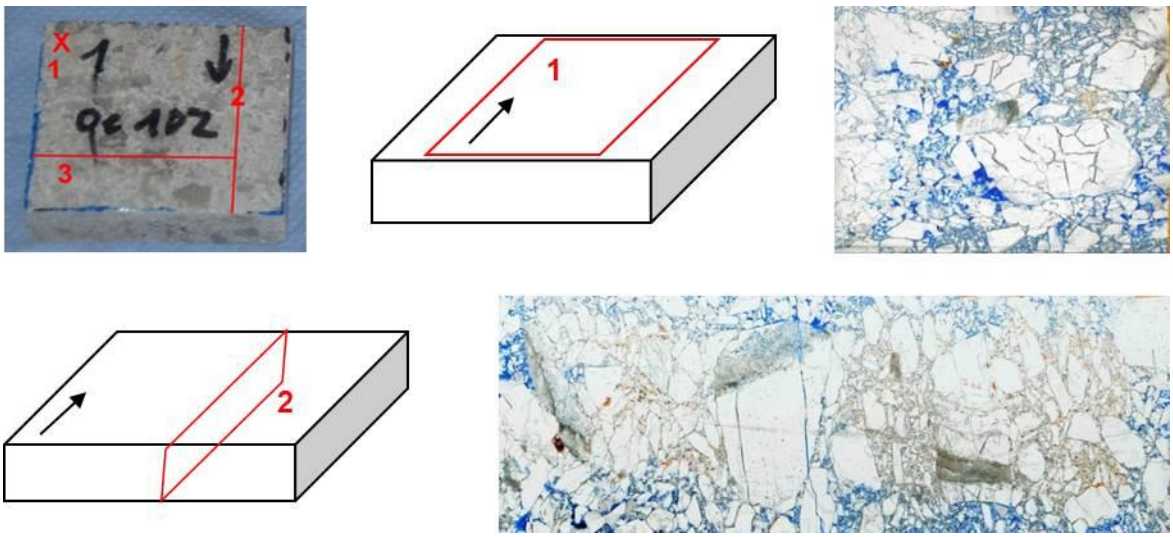

Fig. 2.1: Image of the crushed salt sample used by BGR in oedometer test 102/1 and thin section images of an area close to the surface (thin section 1) of the sample and of a perpendicular cut (thin section 2).

The thin section cut close to the surface (thin section 1) shows that the blue resin has penetrated the crushed salt body across the entire surface of the cut (Fig. 2.1). This shows a completely interconnected pore system. Open pores with sizes of 2-3 mm can be identified, especially where larger salt grains adjoin each other. Only a few isolated, open areas (dyed red) can be made out.

The thin section cut perpendicular to the sample (thin section 2) shows a different situation with a central area that is mostly free of the blue resin but shows a number of red areas, i.e. dead pores. Only a few spots in this central area have been penetrated by the blue resin. These are mostly cracks that run through larger halite grains. Such an area is shown in Fig. 2.2 with a higher resolution. The open pathways along cracks and larger pore spaces are clearly visible. This indicates that the resin was able to penetrate to the core of the sample via grain boundaries and cracks. This may indicate a need to filter out the coarsest grains when defining the grain-size distribution curve or when fabricating the crushed salt in order to reduce fluid paths along grain boundaries. The black spots visible within these pathways are probably small air bubbles that have not been completely removed during evacuation and were enclosed by the blue resin during soaking. They are shown in Fig. 2.3 with an even higher resolution.

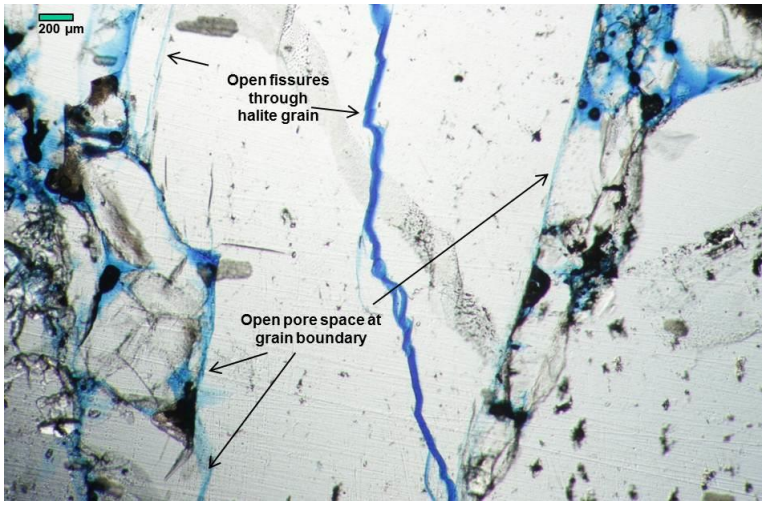

Fig. 2.2:
Enlarged view from the thin section of sample 102/1 (~4.6% porosity) showing main fluid pathways through cracked halite grains and at its boundaries.

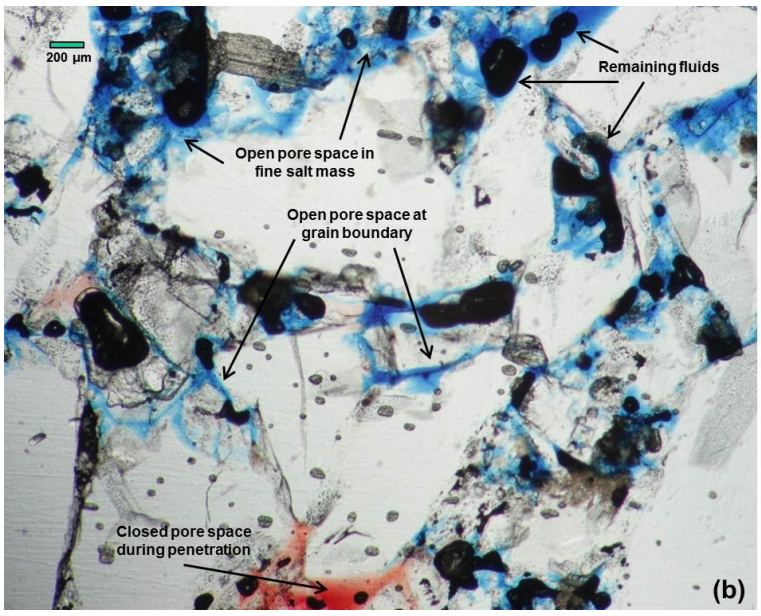

Fig. 2.3:
Enlarged view from the thin section of sample 102/1 (~4.6% porosity) showing open and “dead” pore space as well as bubbles of enclosed fluids

Fig. 2.4 shows an enlarged section of the central area that has not been penetrated by the blue resin. This area shows a number of brine inclusions within the halite grains, especially along dead pores. In addition to this, dead pores dyed red can be identified as well.

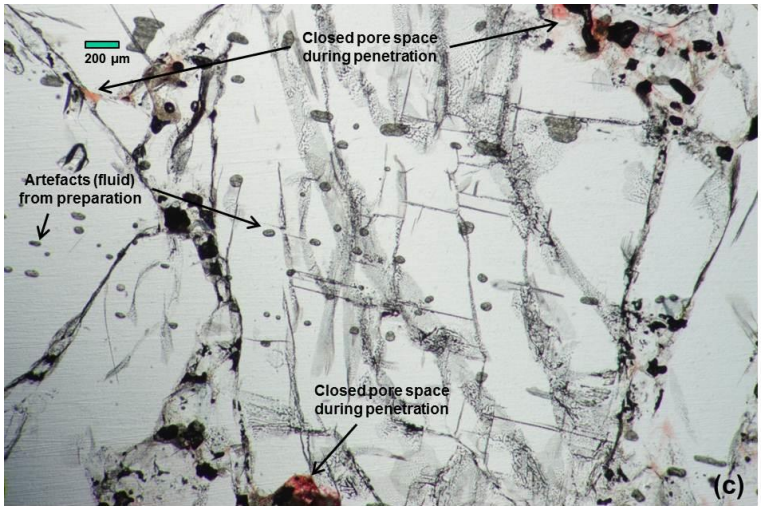

Fig. 2.4:
Enlarged view from the thin section of sample 102/1 (~4.6% porosity) showing dead pores and artefacts from preparation.

Fig. 2.5 shows thin section images of three crushed salt samples that were compacted using different methods. The thin sections were taken parallel to the surface of the samples. Sample 047/5 was compacted in dry condition at 200°C for 78 days and has a void ratio of 0.006. Sample 051/8 was compacted at 100°C for 6 days and has a void ratio of 0.063. Sample 056/5 was also compacted at 100°C for 6 days with the addition of 1.2% salt solution. The images of the thin sections show different characteristics.

The structures of the first two samples shown in Fig. 2.5 are similar, while the third sample looks quite different. It is obvious that hardly any resin penetrated into sample 047/5 (compacted at 200°C), although the thin section was taken close to the sample surface. Contrary to this, the resin is completely distributed in the pore net of the fine grained section of sample 051/8. The third image; i.e. the thin section of sample 056/5, shows a completely different structure. Although the large grains can be seen as well, the fine grained section is not as recognizable as in the two other samples. The addition of 1.2% salt solution during compaction obviously had the effect that the small grains in the fine grained section “bonded’’ so that the amount of fine pores in this section was reduced significantly.

While the first two images show more or less clearly that the resin permeates the samples like a network, such a network cannot be identified in the third image. However, this sample is interspersed with local “hot spots” that seem to be not linked in the plane of the thin-section. (cf. enlarged section). If and to what extent these “hot spots” are linked via a three-dimensional pore system (perpendicular to the thin-section plane) cannot be assessed this way.

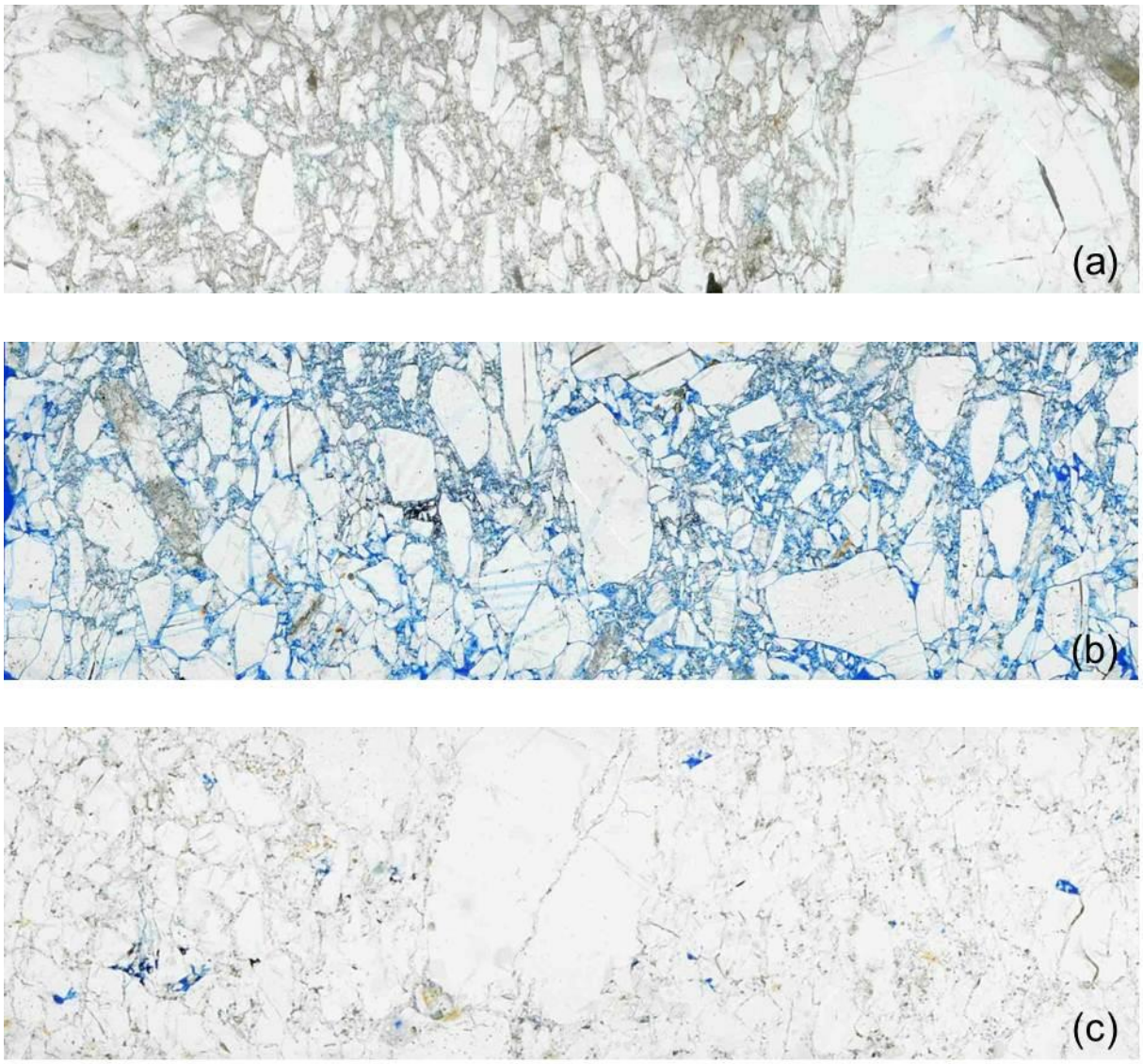

Fig. 2.5: Thin section images of three differently compacted crushed salt samples
(a) Sample 047/5, compacted at 200°C, porosity ~0.6%; (b) Sample 051/8, compacted at 100°C, porosity ~6.3%
(c) Sample 056/5, compacted at 100°C, porosity ~3.1%. and1.2% salt solution added,

Fig. 2.6 and Fig. 2.7 show enlarged areas of the images (a) and (c) in Fig. 2.5. Although sample 47/5 is highly compacted down to a porosity of less than 1% (see Tab. 2.1), it is easy to distinguish between individual grains and the fine salt (grey areas). Larger grains are even “embedded” in the fine salt mass as can be seen in the upper left of the four images. In these highly compacted areas it seems that remaining pathways for a moving fluid through the sample are mainly along the boundaries of larger grains indicated in the lower right image.

Looking at the enlarged areas of sample 56/5 (Fig. 2.7) the picture is completely different. Compared to Fig. 2.6, individual grains can hardly be identified which indicates that additional microstructural processes must have taken place during deformation. Especially when the sample has small but significant amounts of water, recrystallization processes (e.g. fluid assisted grain boundary migration) and solution-precipitation creep (pressure solution) move into focus (e.g. Urai & Spiers, 2007). As can be seen in Fig. 2.7 the microstructure of the fine salt mass

has been altered due to processes specified. These areas have been marked by red circles in the upper two images of Fig. 2.7.

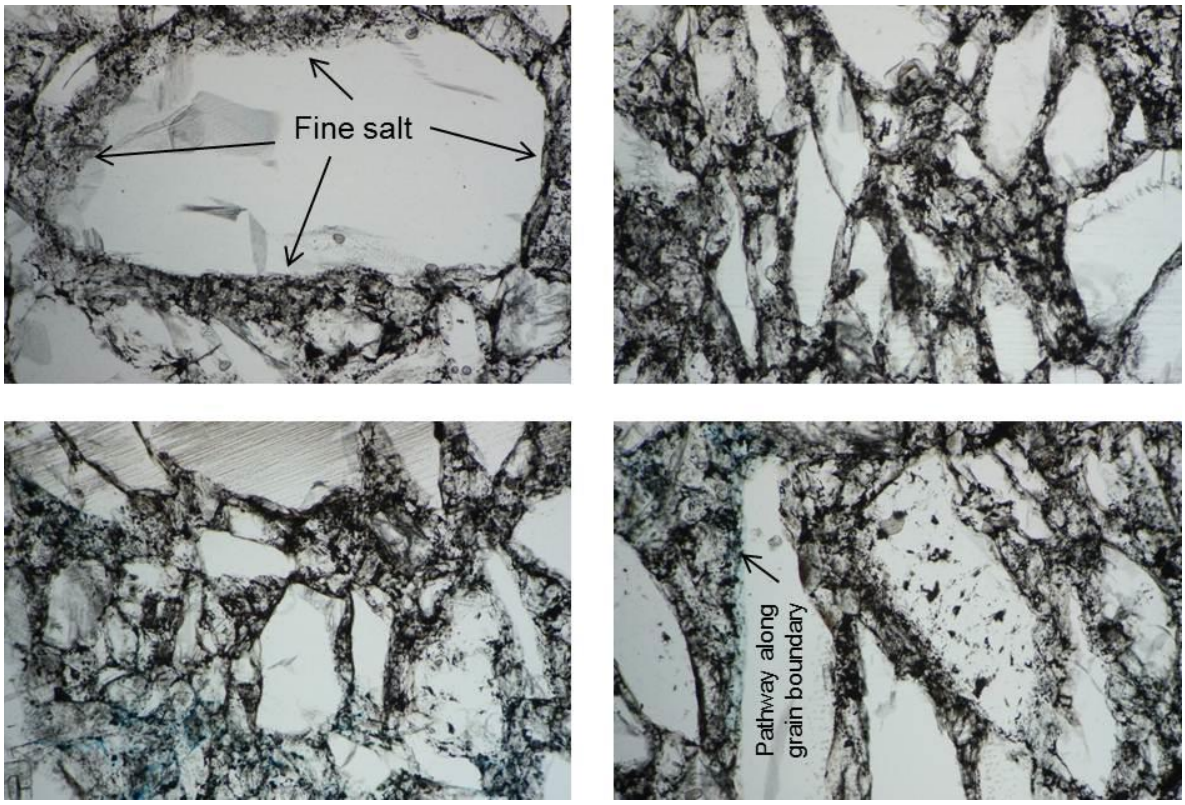

Fig. 2.6: Enlarged thin section areas of the highly compacted sample 47/5.

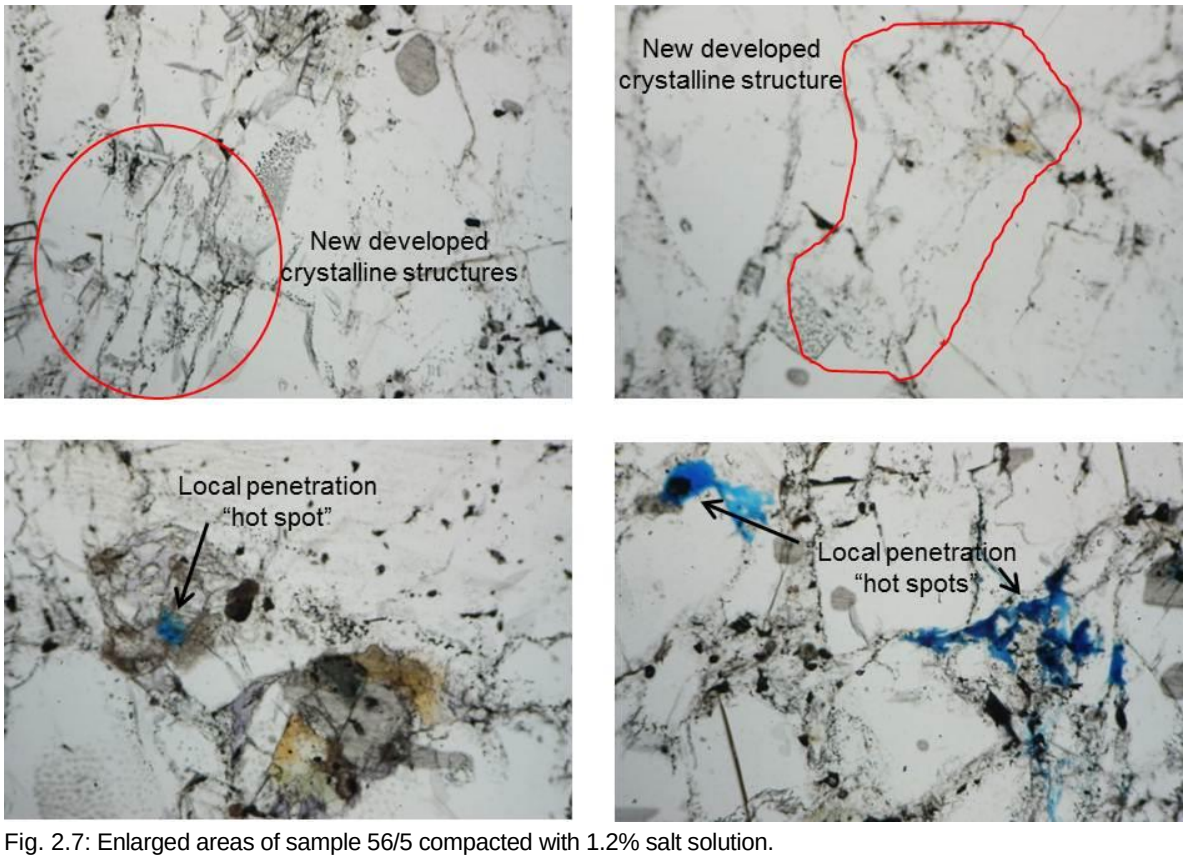

Fig. 2.7: Enlarged areas of sample 56/5 compacted with 1.2% salt solution.

With regard to remaining pathways it can be observed that instead of a fine network local “hot spots” appeared as indicated in the lower two images of Fig. 2.7.

In addition to this, two other samples were investigated. The sample (102/1) was prepared by adding moist air during compaction (Fig. 2.8) and sample D-A-025/2 which was initially compacted in a dry state and subsequently permeated with salt solution in order to determine its permeability to brine (Fig. 2.9).

A comparison of sample 102/1, which had been prepared by adding moist air, with sample 056/5, which had been prepared by adding 1.2% salt solution, shows that the structure of sample 102/1 is similar to those of the samples that were prepared in dry condition but is completely different from sample 056/5 (added salt solution). This means that the addition of moist air is not sufficient to modify the pore system on the fine grain level in such a way that "bonding" or cementation takes plays as does when salt solution is added.

Compared with sample 056/5, the sample that had been permeated with brine after dry compaction (D-A-025/2) shows a lot more “hot spots”. This indicates that leaching took place during permeation, which led to the formation of a “vessel system” that could be permeated by the resin. This vessel system seems to be permanent. With regard to the real situation in a repository where crushed salt is used as backfill material in the drifts, this could indicate that the occurrence of an early brine inflow and pressure build up in the crushed salt; i.e. when it has not yet completely compacted, could lead to the formation of an unwanted system of larger pores which might remain for a certain period of time until it is compacted and closed by the convergence.

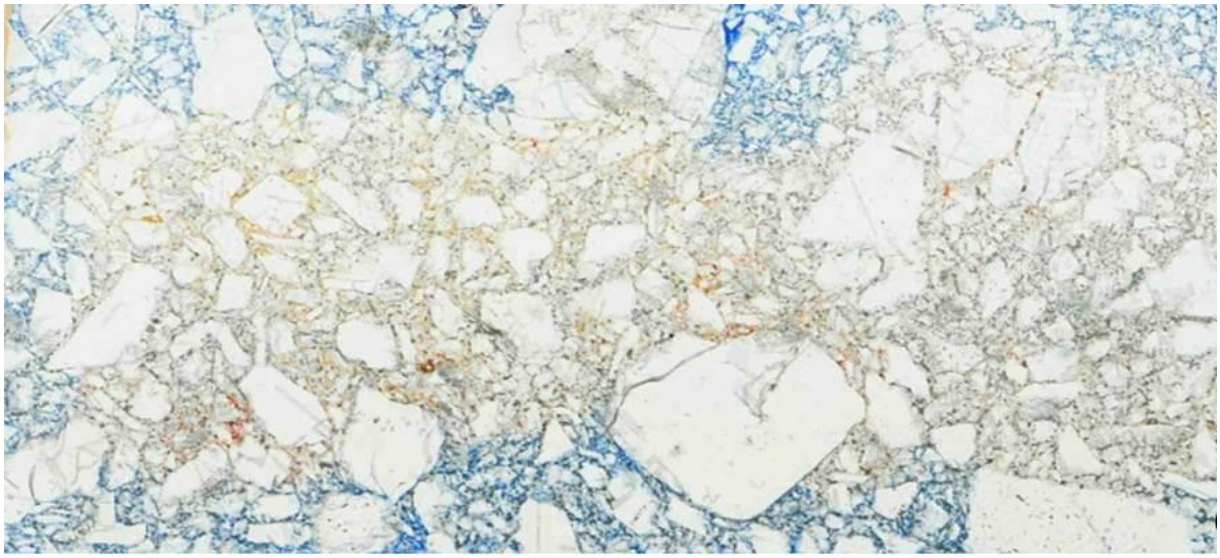

Fig. 2.8: Thin section images of the crushed salt sample 102/2 compacted at ~33°C with moist air added during compaction, porosity ~4.6%

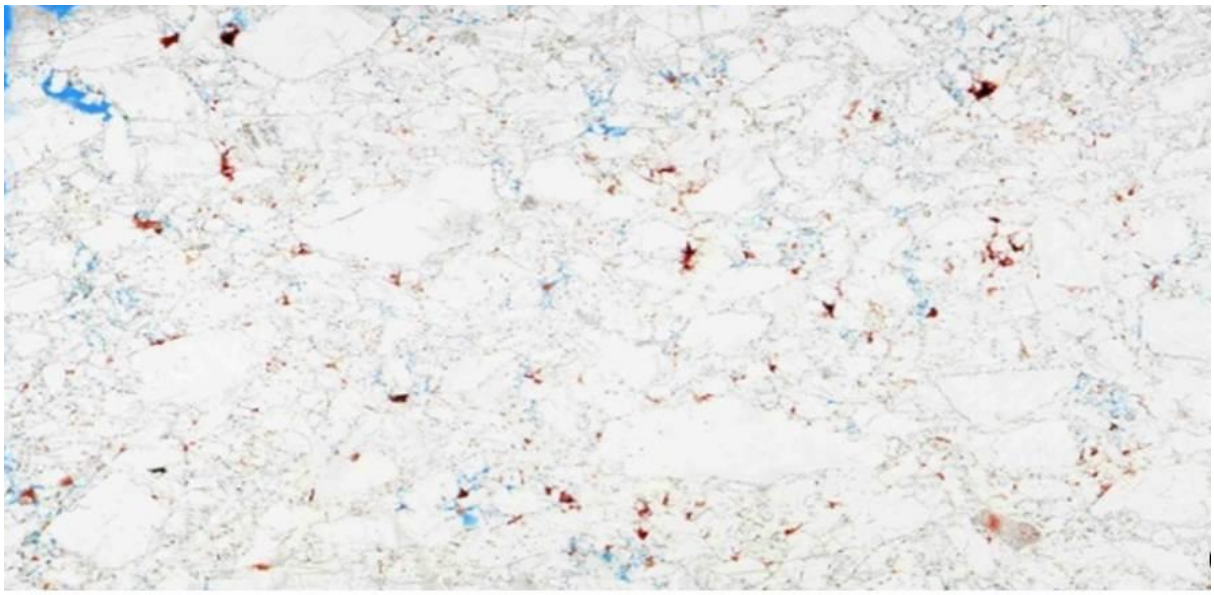

Fig. 2.9: Thin section images of the crushed salt sample D-A-25/2 initially compacted in a dry state and subsequently permeated with salt solution.

2.2 Computer tomographic analyses

So far tomographic investigations of compacted crushed rock salt are scarce. In-situ XCT (X-ray Computer Tomographic) measurement during compaction of pure halite allowed the reconstruction of 3D microstructures corresponding to stages of increasing deformation (Renard et al. 2007). These authors showed that increasing deformation (i.e. pressure solution creep) caused reduction in porosity and related decrease in permeability. Thereby, it should be recognized that permeability changes due to porosity changes are particularly pronounced near the critical porosity (percolation threshold) as it was for example demonstrated for Opalinus Clay (Keller et al. 2013). The relationship between fundamental microstructural properties such as the percolation threshold and degree of compaction are vital when assessing the sealing properties of compacted crushed rock salt.

The aim was to investigate whether tomographic methods together with percolation theory can give indications about a critical porosity of crushed rock salt that, once reached, doesn't allow any more permeation.

To assess these sealing properties of crushed rock salt we used XCT and FIB-nT (Focussed Ion Beam nano Tomography) in order to obtain 3D reconstructions of the macroporosity (radii > 4 µm) and microporosity (radii < 1 µm). Some details of resolution effects of XCT can be found in Peng et al. (2012). The reconstructed pore microstructures were then analysed with respect to homogeneity, percolation properties and representativity using the same procedure that was recently applied to Opalinus Clay (Keller et al. 2013).

The two samples 47/5 and 51/8 (Tab. 2.1) with different degrees of compaction were examined.

2.2.1 Sample preparation

FIB-nt: Salt slabs with a thickness of around 1 mm were cut with the help of a saw with a thin (thickness of saw blade = 200 µm) diamond blade. Afterwards the slaps were lightly sanded to remove material that was damaged during sawing. To stabilize the salt slabs, they were sandwiched between two 50 µm thick glass discs, which were glued together with epoxy. Then, a cross-section was cut with a diamond saw. The surface of this cross-section was polished locally by using a Hitachi IM 4000 broad ion beam (BIB) instrument. The polished area was subsequently investigated by SEM (Scanning Electron Microscope) and FIB-nt. SEM imaging of BIB polished crushed rock samples is used for a material characterization on the mm-scale (for comparison: typical sample size of the FIB-nt analysed volume is a cube of 10-30 µm edge length). BIB polishing occurred at 6keV for 1.5 h.

XCT: Salt prisms with ground areas of around 3x3 mm and heights of about 5-10 mm were cut with a diamond saw and were subsequently lightly sanded to remove material that was damaged during sawing. XCT scans were then performed in the centre of the material in order avoid artefacts related to mechanical sample preparation.

2.2.2 X-ray Computer Tomography (XCT)

The prepared millimeter size prisms were analyzed by XCT in order to explore the micron-scale pores. Two XCT scans per sample were performed in the center of the material in order avoid artifacts related to mechanical sample preparation. The following set up was used to analyze the salt samples. The samples were scanned with a X-ray micro tomography cone beam setup consisting of a µm spot size X-ray tube “XT9160-TXD” from Viscom, a rotation table “UPR-160F air” from Micos and a X-ray flat panel detector “C7942 CA02” from Hamamatsu covered with a 1 mm thick Al plate. A voltage of 40 kV was applied to accelerate the electrons which impacted on a tungsten target with diamond support.

The projection images were taken at angles uniformly distributed over 2π, whereby the last projection served to determine the quality of the measurement (the projections at 0 and 2π should be equal). To correct for dark counts and inhomogeneity of the detector a dark and a flat image were acquired with total integration times of 32 s and 64 s, respectively. The projection images were corrected for bad pixels, beam hardening and ring artifacts before a standard filtered backprojection algorithm was used for reconstructing the 3D absorption image. Based on the detector pixel size and the magnification, the resulting voxel edge length of the reconstructed 3D image was 4 µm.

2.2.3 Focused Ion Beam nano-Tomography

FIB-nt was done with a dual beam FIB-SEM instrument, in which an ion beam and an electron beam focus intersect at a point on the sample surface. 3D information can be obtained by acquiring a sequence of cross sectional images spaced evenly through a region of a bulk specimen, and reconstructing those two-dimensional images into a three-dimensional representation of the sampled volume. The process begins by the milling of a wedge shaped trench in the sample. One wall of the trench is vertical (i.e., normal to the specimen surface) and becomes the initial cross section imaged by the electron beam. After imaging, the ion beam is used to remove a layer of uniform thickness of material from this wall, advancing the

cross section a predetermined distance through the sample volume. Another electron image is collected. By repeating this milling/imaging process, the cross section advances through the targeted volume, which results in a stack of 2D images. One image stack for each analyzed sample was collected.

2.2.4 Image processing

X-ray tomography

The background of the images was corrected by using a 3D in-house image filter. A mean shift filter was then applied to reduce the noise in the images. Grey-level contrast thresholding allowed an accurate segmentation of pores, a specific mineral which is assumed to be anhydrite with bright contrast and a matrix consisting of salt minerals. Based on the segmented image stack the pore space was visualized by using the Avizo software.

FIB-nt

The SEM images were aligned by using the algorithm implemented in the image processing software called “Fiji”. Then, the maximal overlapping area was cropped from the images of the aligned SEM image stacks. Vertical stripes in the images which are artifacts of ion milling (i.e. the so-called waterfall effect) were then eliminated by applying an in-house destriping filter. Then, a 3D background correction was applied in order to reduce systematic large-scale intensity variations which are caused by shadowing effects related to the oblique imaging angle and to the subsidence of the image plane into the milled trench.

The reconstruction of a 3D microstructure requires a segmentation of the images, i.e. the pores have to be located in the images. Due to weak image contrast, the pores were manually segmented from the SEM images using the tools for manual segmentation provided by the Avizo software. For 3D visualization, we used the “Avizo” software.

2.2.5 Results

Micro- to macro-scale pore structures based on BIB and SEM imaging

SEM images on the hundreds of micron scale and SEM images at higher magnifications of the prepared samples are shown in Fig. 2.10 and Fig. 2.11. The SEM images reveal that the examined samples contain nano-scale (micropores) and micron-scale pores (macropores). The geometry of the macropores is defined by geometric incompatibilities between angular salt grains. Geometric compatibility between grains is higher in sample 47/5 when compared to sample 51/8, which results in a lower porosity and connectivity in sample 47/5. Micropores are located in compact grain aggregates, mainly along grain boundaries but also in the interior of grains. In 2D these pores have a circular shape and can be seen as fluid inclusions.

Macro-scale pore structure based on XCT

3D reconstructions of the analyzed samples (047/5 and 051/8) and pore space reconstructions are shown in Fig. 2.12 and Fig. 2.13. The reconstructed samples are on the upper left image (a) and the reconstructed pore spaces are on the upper right images (b). The light grey objects in the reconstructed samples have been identified as anhydrite and its distribution is shown in the lower images (c).

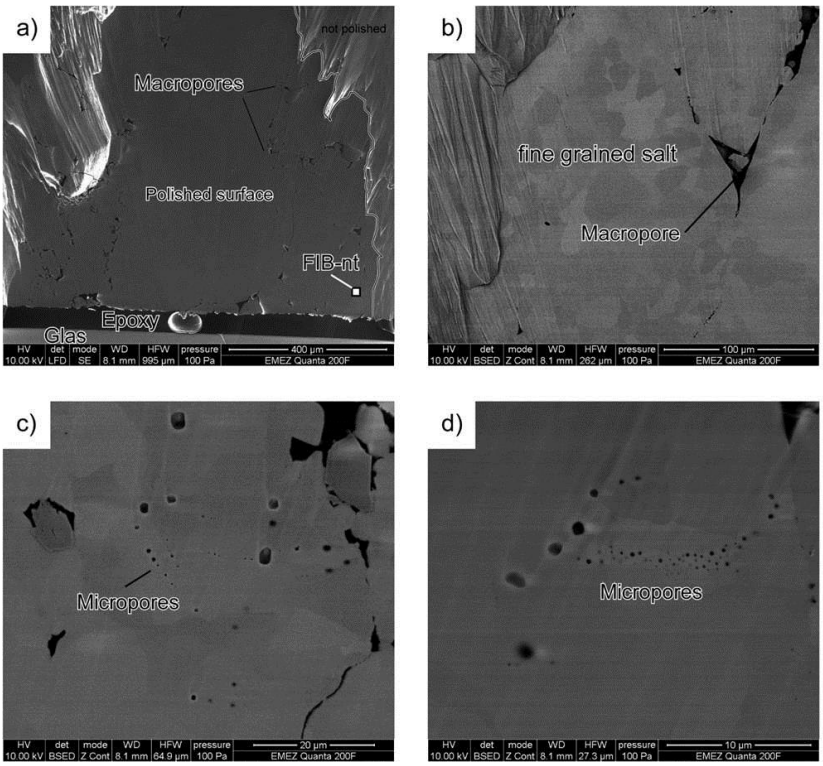

Fig. 2.10: SEM images at different magnifications of sample 47/5. a) Overview of the area, which was polished with help of a BIB instrument. b) Orientation contrast between individual salt grains. The image shows that the compact areas are in fact grain aggregates and not single crystals. c) and d) Images at higher magnifications document micropores in otherwise compact grain aggregates.

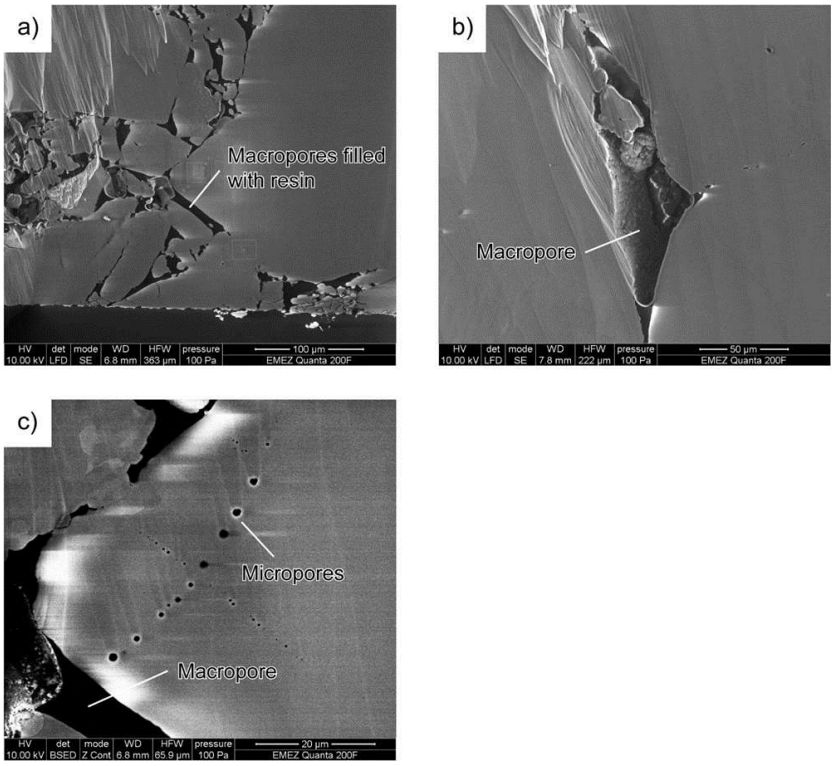

Fig. 2.11: SEM images at different magnifications of sample 051/8. a) Overview of the area, which was polished with help of a BIB instrument. b) Orientation contrast between individual salt grains. The image shows that the compact areas are in fact grain aggregates and not single crystals. c) Image at higher magnifications document micropores in otherwise compact grain aggregates.

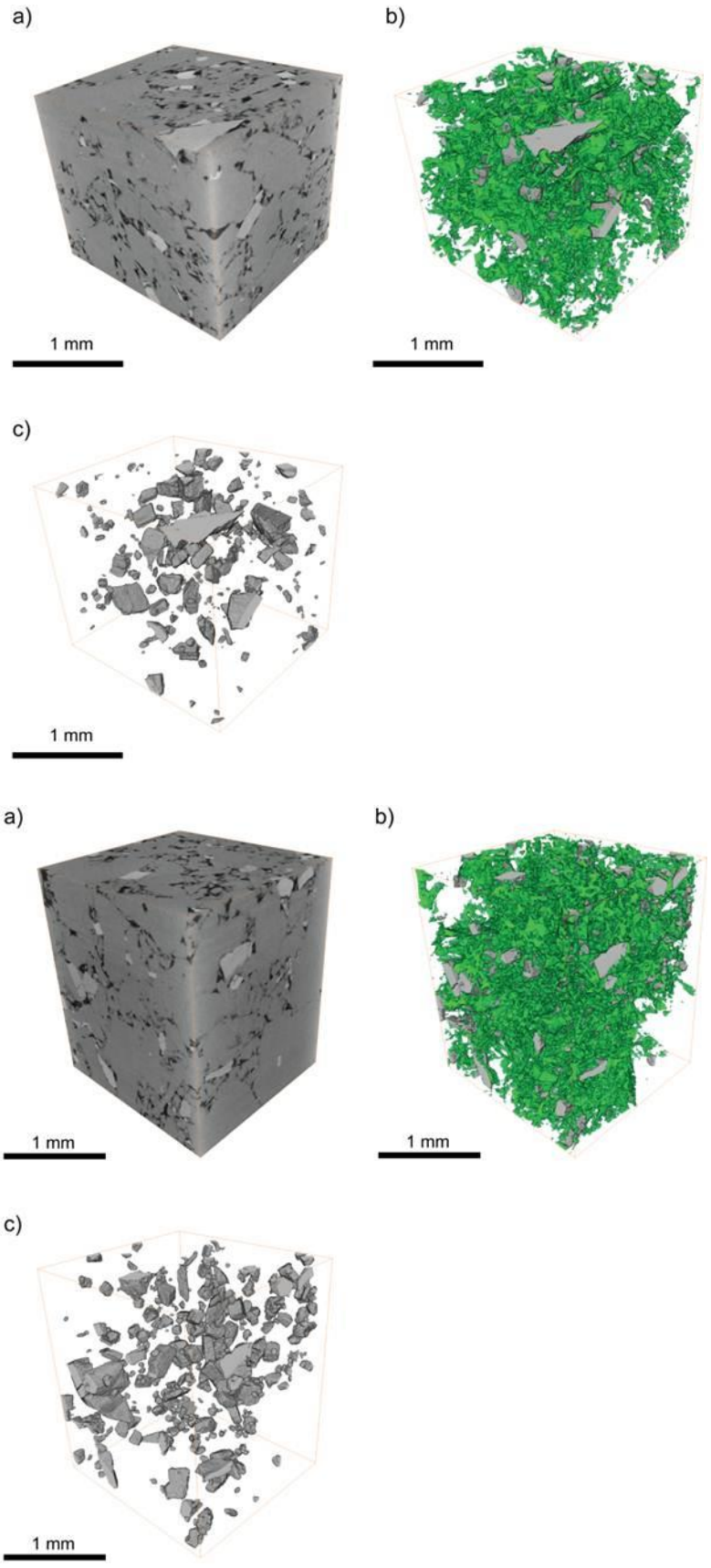

Fig. 2.12: Visualization of two XCT data sets of sample 051/8. a) 3D reconstruction of the analyzed volume. b) 3D reconstruction of pore space (green) and the anhydrite mineral with bright image contrast (grey). c) Reconstruction of anhydrite distribution.

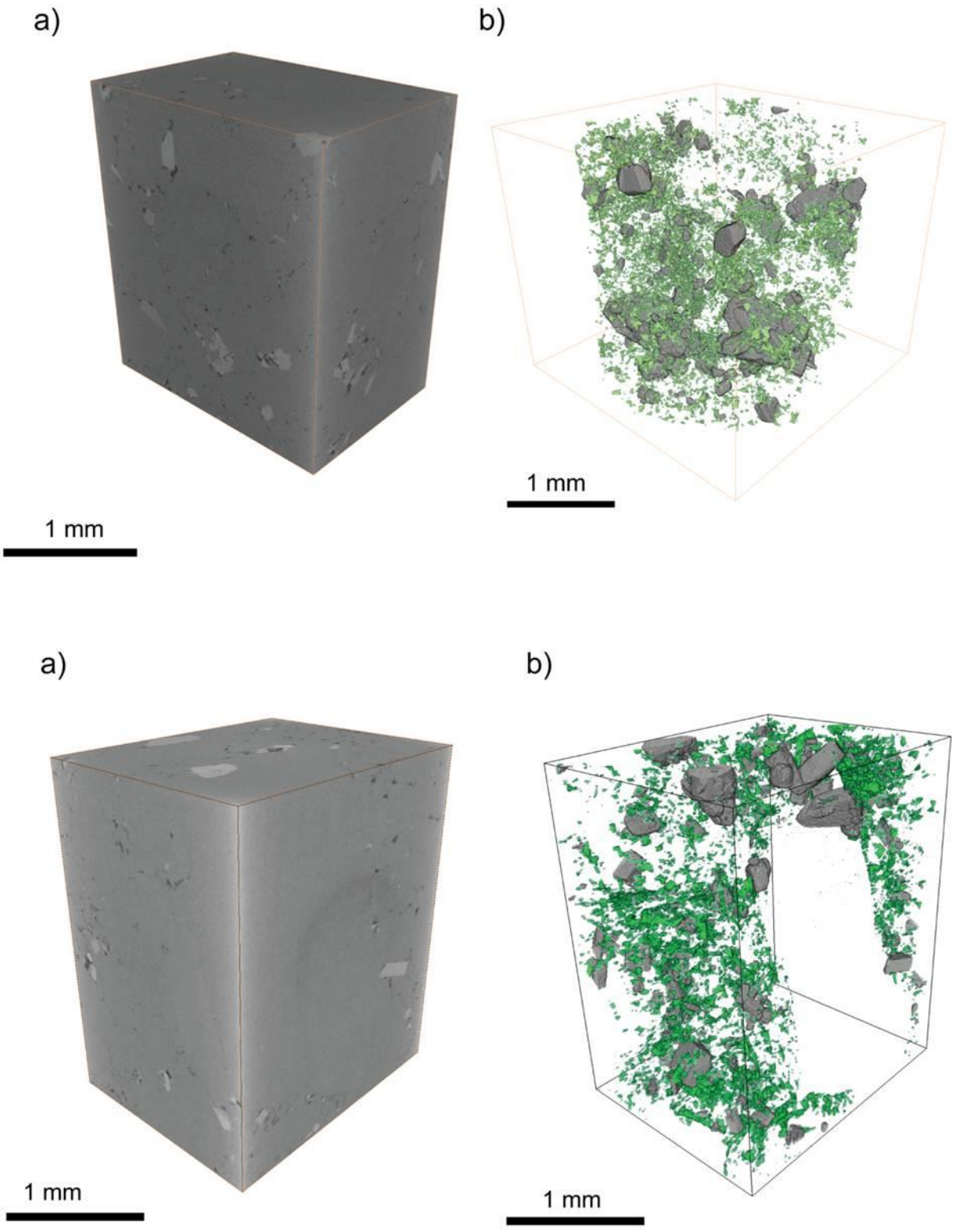

Fig. 2.13: Visualization of two XCT data sets of sample 47/5 a) 3D reconstruction of the analyzed volume. b) 3D reconstruction of pore space (green) and the anhydrite mineral (grey).

Regarding sample 47/5 (Fig. 2.13), the porosity related to pores with radii > 4 µm is around 1 vol. % and the pore space consist of numerous isolated pore objects. Substantially higher macro porosity (~10 vol. %) was found in sample 051/8 (Fig. 2.12).

The samples differ also with respect to pores size distribution. Continuous pore size distributions calculated on the base segmented image stacks (Münch & Holzer 2008) are shown in Fig. 2.14. The majority of pores in sample 47/5 have radii < 20 µm and the most frequent pore radii is around 10 µm. Sample 051/8 contains larger pores with radii < 40 µm and the most frequent pore radii is around 15 µm and is thus, similar to the one of sample 47/5.

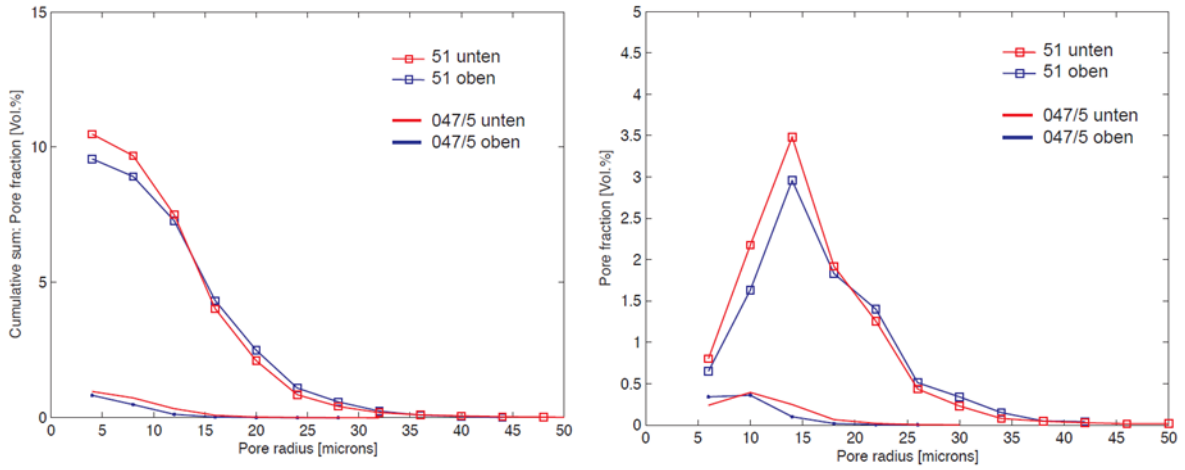

Fig. 2.14: Compilation of continuous pore size distributions for the two different compacted crushed salt samples, which are based on 3D data from XCT. (left) Cumulative distribution, (right) corresponding differential distribution showing the main observed pore radii in the samples.

Micro-scale pore structure based on FIB-nt

3D reconstructions of the analyzed volume and 3D reconstructions of the pore space are shown in Fig. 2.15 and Fig. 2.16. The analyzed volumes contain a small number of pores with radii < 1 µm (Fig. 2.17) and a porosity in the 0.2 to 1.0 vol. % range. On the size of the analyzed volumes, micropores are inhomogenously distributed and the pore size distributions of the two samples are therefore difficult to compare and are thus, given as relative distributions (i.e. normalized so that porosity sums one) (Fig. 2.17). Both, the cumulative and the differential distribution indicate that sample 51 only contains a limited amount of pores on the nanometer scale. No pores of a size between 500 nm and 1 µm were found. Sample 47/5 however contains pores distributed among the whole nanometer scale.

Often crystal planes define the pore shape, which in the case of salt results in a cubic or circular pore geometry (Fig. 2.15). On the scale of observation, these pore objects are spatially isolated (fluid inclusions) and do not touch each other (Fig. 2.15, Fig. 2.16). Such micropores occur in-plane along grain boundaries or within the grain as fluid inclusions (Fig. 2.16) and at grain triple points. The orientation contrast between salt grains visible in SEM images gives an idea of the sub-grain size of such aggregates (Fig. 2.15). Within the analyzed volume the sub-grain size ranges between a few microns to tens of microns.

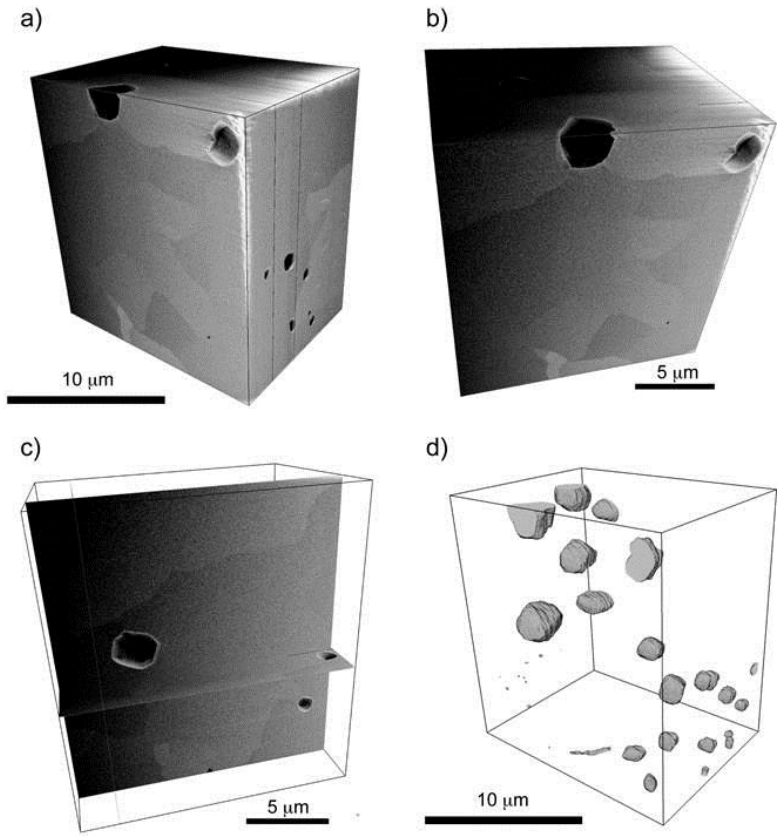

Fig. 2.15:
Visualization of the FIB data set of sample 47/5. a), b) and c) 3D reconstructions of the analyzed volume documenting the granular pore geometry . d) 3D reconstruction of pore space.

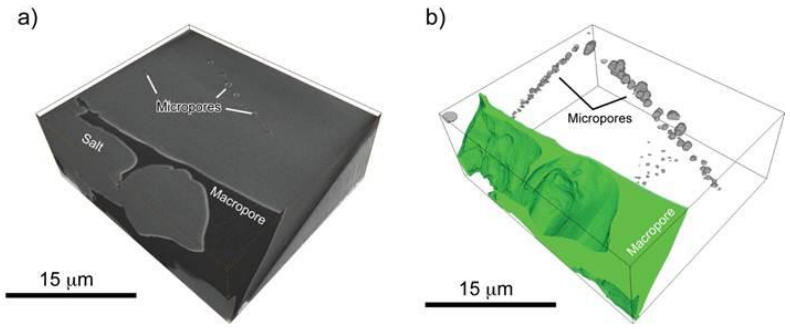

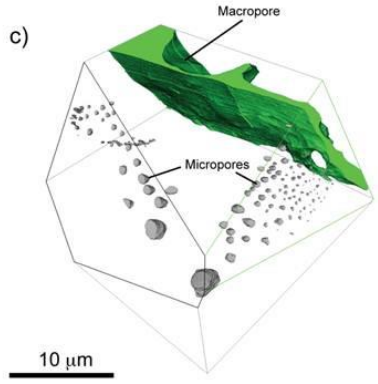

Fig. 2.16:
Visualization of the FIB data set of sample 051. a) 3D reconstructions of the analyzed volume, b) 3D reconstruction of pore space showing a macropore and numerous in plane fluid inclusions, c) 3D reconstruction of pore space documenting that the micropores or fluid inclusions are aligned in planes (i.e. sub-grain boundaries).

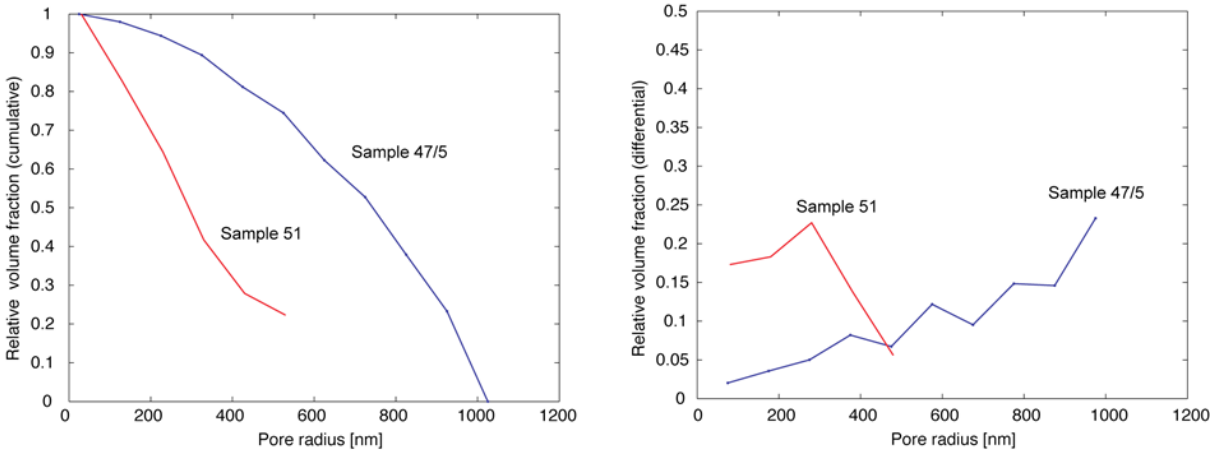

Fig. 2.17: Relative (i.e. normalized so that porosity sums one) continuous pore size distributions of microporosity in samples 47/5 and 051 based on 3D data from FIB with a) cumulative distribution and b) corresponding differential distribution.

2.2.6 Local porosity analyses

To characterize the heterogeneity of the pore structure and to evaluate the representativeness of tomographic methods the local porosity theory to the reconstructed pore structures were applied. The local porosity theory pursues to define the probability density functions of porosity and porosity connectivity (see appendix and Keller et al. (2013) for further details). The local porosity distributions $\mu(\Phi,L)$ corresponding to the macroporosity are shown in Fig. 2.18. The function $\mu(\Phi,L)$ *measures the probability to find the local porosity* Φ *in the range of* Φ *to* $d\Phi$ *in a cell of linear dimension L. Details can be found for example in Hu & Stroeven (2004) and Hilfer (2000).* With increasing L the μ curves change from a wide distribution to a distribution with a single peak at the position of the bulk porosity. Development of a single peak occurs for cells with edge lengths L > ~700 µm. This means that at millimeter length scale there is a high probability to find a local porosity that equals the bulk porosity, which in turn can only be true if the pore space possesses a certain degree of homogeneity. In addition, the function component at the origin decreases with increasing L (Fig. 2.18). All these indicate that similarities between local geometries increase with increasing L. It also indicates that the macro-porosity possesses a certain degree of homogeneity on that scale.

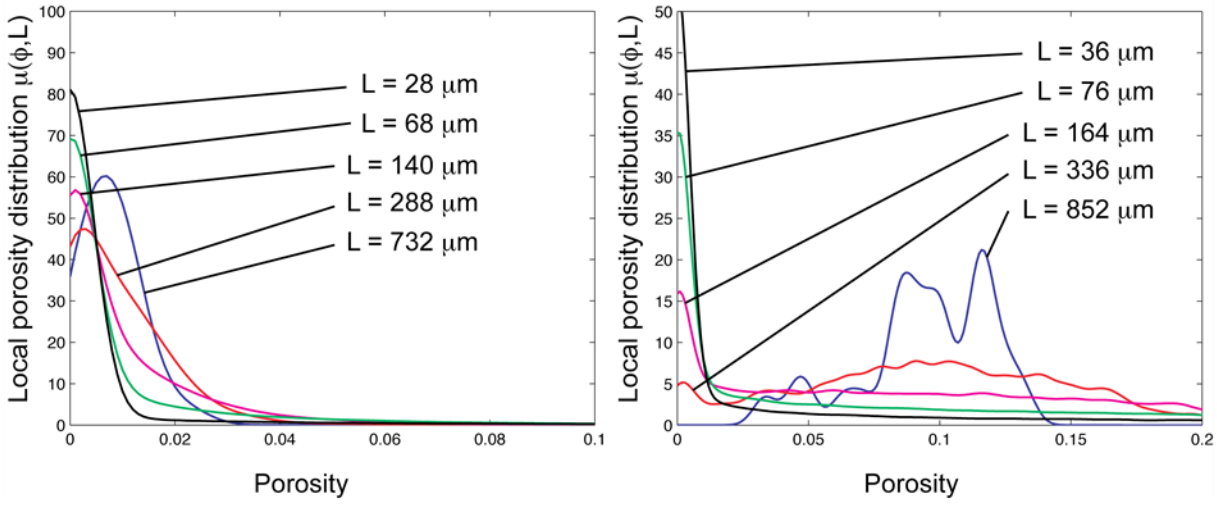

Fig. 2.18: Local porosity distributions calculated for different length L of measuring cell and on the base of XCT data. Sample 47/5 (left), Sample 51(right).

The local porosity distributions $\mu(\Phi,L)$ (see appendix) corresponding to the microporosity of sample 47/5 are displayed in Fig. 2.19. For sub-sample sizes up to around 4.8 µm, the µ curves have high function components at the origin and the distribution is “smeared-out” over a wide range of porosities. This indicates that the pore structure does not possess homogeneity on the sample size that can be analyzed by FIB-nt. However, similarities between local pore space geometries increase with increasing *L*. Due to the lack of homogeneity and strong geometrical arrangement of micropores (fluid inclusions), local porosity theory was not applied to sample 051.

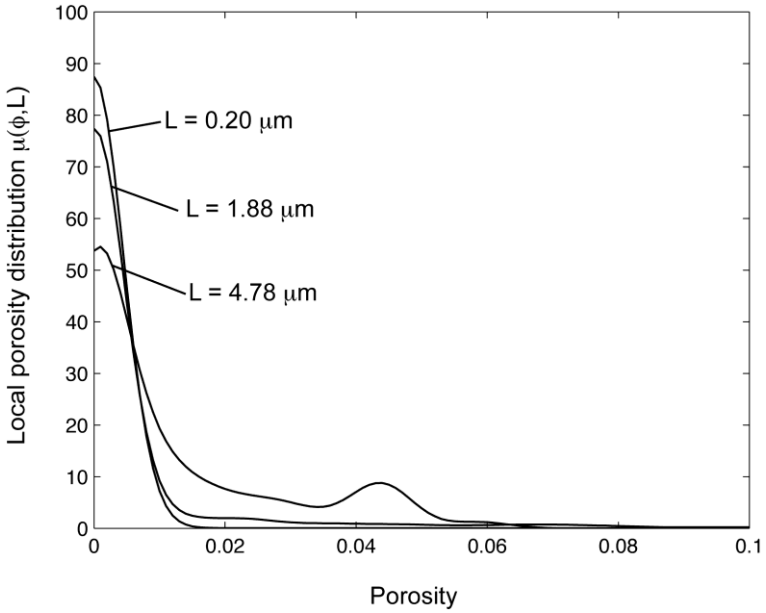

Fig. 2.19:
Local porosity distributions calculated for different length L of measuring cell and on the base of FIB-nt data (Sample 47/5).

2.2.7 Local percolation analyses

Regarding two-phase flow where for example a gas phase is forced into a water saturated pore space and water is replaced by gas, gas flow occurs along larger pores because capillary forces required to replace water are lower along larger pores. Thus, percolation and connectivity of the resolved pore space is of interest. These transport properties can be assessed by calculating the percolation probability λ(Φ,L), which is the fraction of cells with local porosity Φ and side length L, containing a pore network that is percolating along a specific transport direction.

Calculated percolation probabilities $\lambda_\alpha(\Phi,L)$ related to macroporosity are displayed in Fig. 2.20. Smooth curves are fitted curves, which were used as input for the calculation of the percolation threshold (see below). One notices that macroporosity is isotropic in its connectivity as it is indicated by similar positions of λ curves corresponding to different spatial directions. The relative position between bulk porosity and the position of the λ curves gives an idea of the connectivity of the pore structure. Regarding sample 47/5 major connectivity changes occur at much higher porosities (i.e. > 0.05) when compared to the bulk porosity (i.e. ~0.01) of the sample. This indicates that macropores are poorly connected. On the contrary, for sample 51 major connectivity changes for subsample sizes occur at similar porosity values as the bulk porosity (i.e. ~0.1) of the sample. This indicates good connectivity of the sample.

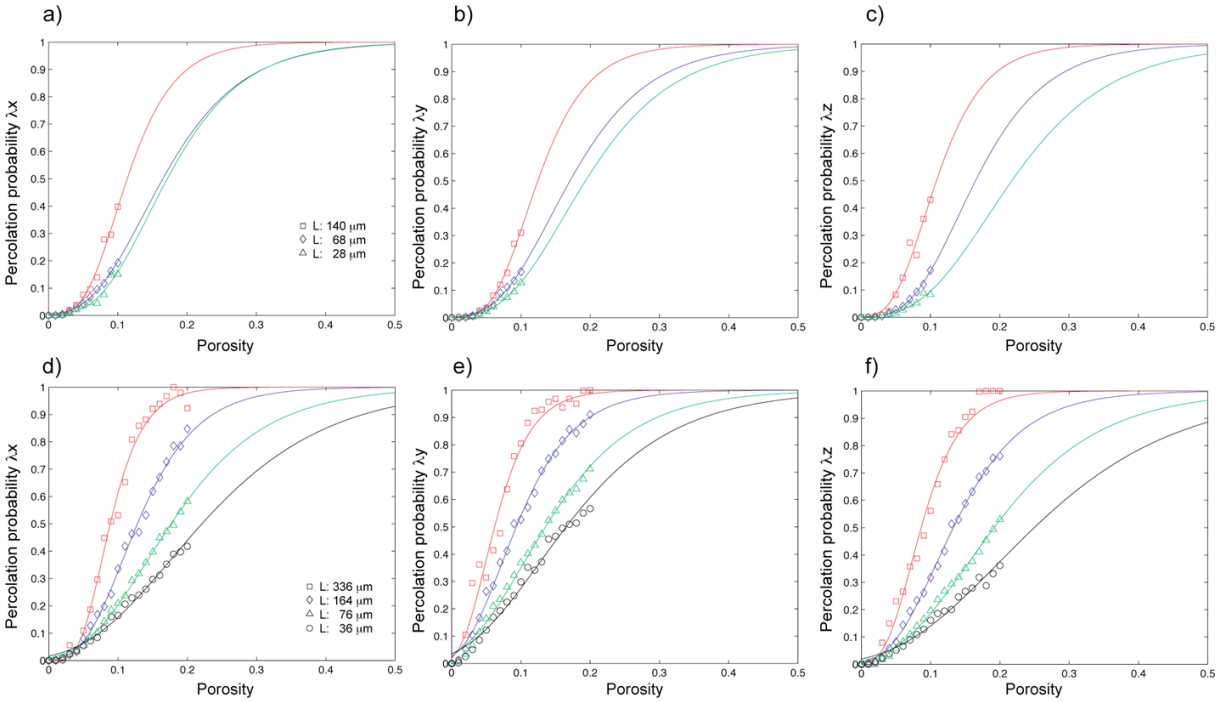

Fig. 2.20: Percolation probabilities of macroporosity along different directions. Symbols are computed values and lines smooth interpolations. a) Sample 47/5: x-direction, b) Sample 47/5: y-direction and c) Sample 47/5: z-direction. d) Sample 051: x-direction, e) Sample 051: y-direction and f) Sample 051: z-direction.

The microporosity is isotropic in its connectivity as indicated by the similar position of the λ curves (Fig. 2.21). At length scales of subsamples, major connectivity changes occur at much higher porosities when compared to bulk porosity (i.e. ~0.01) (Fig. 2.19 and Fig. 2.21). This indicates poor connectivity of the pore structure as it can be expected from visual inspection of the pore structure. In addition, in Fig. 2.21 it can be seen that the transition from unconnected to full connectivity widens with increasing sample size *L*, which is the opposite behavior when compared to macroporosity (Fig. 2.20) (see below). The small numbers of isolated and granular pore objects can explain this behavior because only small measuring cells (*L* ~ 200 nm) can frequently be placed in such pore objects. This increases percolation probability for small sample sizes, whereas for larger samples connectivity is very low as it can be expected on the base of visual inspection of the pore structure.

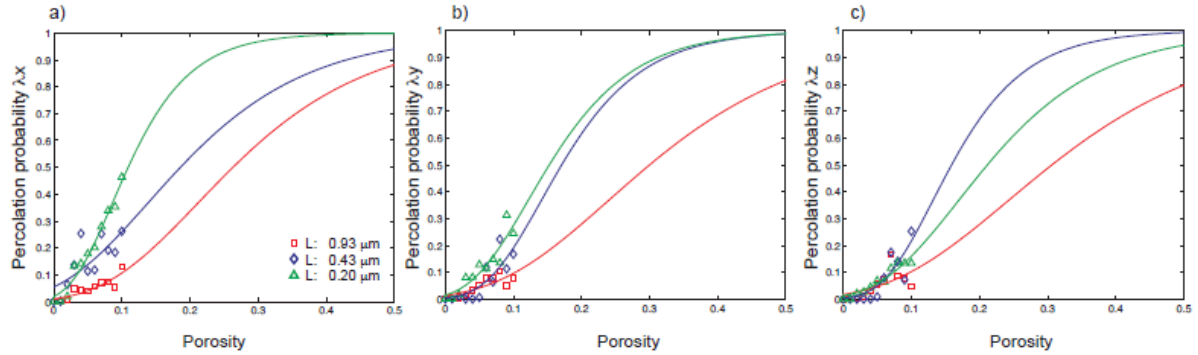

Fig. 2.21: Percolation probabilities of microporosity in sample 47/5 along different directions. Symbols are computed values and lines smooth interpolations. a) x-direction, b) y-direction and c) z-direction.

2.2.8 Percolation threshold

The critical porosity at which one can expect a percolating pore network is a crucial parameter. Here, two finite-size scaling schemes were used in combination with the results obtained from local percolation analysis (Pringle et al. 2009; Keller et al. 2013).

Percolation threshold based on finite-size scaling

The calculated percolation probability $\lambda_\alpha(\Phi,L)$ can be regarded as the probability that a sample with a given porosity Φ and size L percolates along a direction α (Stauffer & Aharony 1995). For infinite (i.e. large L) L and if Φ is below a critical value Φ_c (critical porosity) there is no percolating path across the sample, whereas for small L it is possible to find a percolating path even if $\Phi<\Phi_c$. This is the present situation for the macroporosity of sample 47/5 where $\lambda_\alpha(\Phi<\Phi_c) = 0$ for the sample size that can be analyzed by XCT. For sub-volumes, however, $\lambda_\alpha(\Phi,L)$ was found to be > 0. The question is how can the critical value Φ_c (i.e. percolation threshold) be determined for an infinite sample from the calculated $\lambda_\alpha(\Phi,L)$ curves related to small values of L.

Regarding percolation theory, this can be done by a technique known as finite-scaling (Stauffer & Aharony 1995). For an infinite sample, $\lambda_\alpha(\Phi,\infty)$ is a step function with $\lambda_\alpha(\Phi<\Phi_c)=0$ and $\lambda_\alpha(\Phi>\Phi_c)=1$. This transition widens as sample size decreases (Fig. 2.20). Fig. 2.20 shows that the porosity range of the samples does not cover full transition from $\lambda_\alpha(\Phi,L) = 0$ to 1 for all L. To improve the covered porosity range and to avoid influence of local percolation fluctuations smooth curves fitting to the data have been analyzed (see also Pringle et al. 2009). The derivation $d\lambda(L)/d\Phi$ is essentially the probability to find a percolating sample of size L with porosity Φ on the first trail (i.e. probability for first occurrence) (Stauffer & Aharony 1995). If we define the effective percolation threshold as the porosity with maximum probability Φ_{max} for first occurrence, Φ_{max} can be found by calculating the point of inflection of $\lambda(\Phi)$ (i.e. porosity with maximum of $d\lambda/d\Phi$) (Stauffer & Aharony 1995; Pringle et al. 2009). For an increasing sample size L, percolation transition occurs in an increasingly smaller porosity range which reduces to a single value Φ_c for infinite large samples. Accordingly, for large L $d\lambda/d\Phi$ develops into a peak, of which position Φ_{max} approaches Φ_c. The peak position converges to Φ_c as:

$$\phi_{max} - \phi_c \propto L^{1/\nu} \tag{2.1}$$

where ν is the critical exponent of the correlation length, which has a universal value depending only on the system dimension and in 3D ν = 0.88 (Bunde & Havlin, 1995); Pringle et al. 2009). Fig. 2.22 shows a plot of numerically calculated Φ_{max} vs. $L^{-1/\nu}$. $L^{-1/\nu}$ decreases with increasing L, which implies that for $L\rightarrow\infty$ the value for the infinite size limit is given by the vertical axis intercept (Pringle et al. 2009). A linear least square fit yielded an intercept values for percolation in different directions (Fig. 2.22 and Fig. 2.23). A similar behavior is shown by Φ_{av}, the average porosity at which a percolating cluster appears for the first time. This is defined by (Stauffer & Aharony, 1995)

$$\Phi_{av} = \int_0^1 \Phi \left(\frac{d\lambda}{d\Phi}\right) d\Phi \tag{2.2}$$

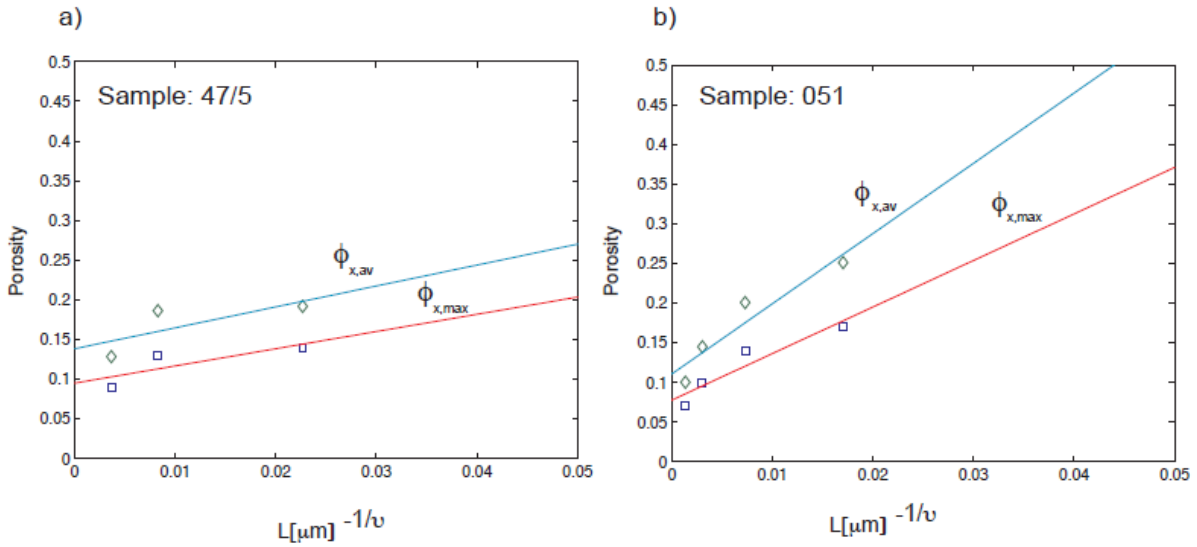

Fig. 2.22: a) $\Phi_{c,max}$ and b) $\Phi_{c,av}$ vs. $L^{-1/\nu}$. Lines are least square fits of which intercept values are given in the plots and are considered as percolation thresholds along x-direction. Similar plots are obtained for other spatial directions.

Then, a similar scaling scheme (i.e. Φ_{av}-Φ_c= $L^{-1/\nu}$ as for Φ_{max} is applied (Pringle et al. 2009). Numerically calculated values of Φ_{av} are plotted vs. $L^{-1/\nu}$ and a linear least square fit yielded an intercept values for the different percolation directions (Fig. 2.22, Fig. 2.23).

Concerning the macroporosity of sample 47/5, the calculations yielded values for the percolation threshold in the 0.08 – 0.14 porosity range. Values along axes in different directions and calculated with a specific scaling scheme do not differ much (i.e. ~ 0.02) indicating near isotropic space geometry (Fig. 2.23). The calculated values are substantially higher than the bulk porosity, which documents the poor connectivity of the pore space.

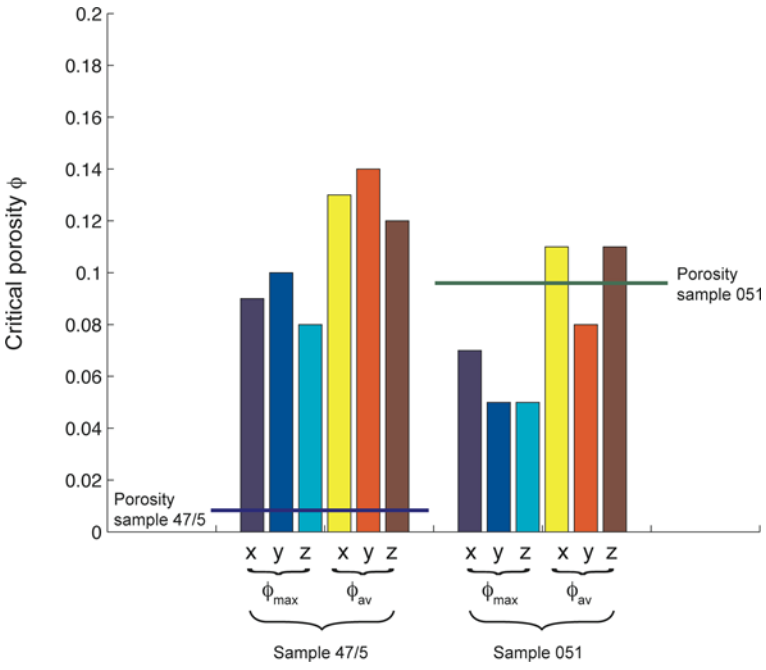

Fig. 2.23: Bar plot shows a compilation of the calculated percolation thresholds related to macroporosity for all samples. The values related to different percolation directions (x,y,z) are grouped according to the applied scaling scheme (i.e. Φ_{max} and Φ_{av}).

Regarding sample 051 the calculations yielded values in the 0.05 – 0.11 porosity range but values related to a specific scaling scheme do not differ much (i.e. ~ 0.03) which indicates a near isotropic space geometry (Fig. 2.23). Critical porosities are lower than bulk porosity, which indicates good connectivity of macropores in sample 051. Regarding the microporosity of sample 47/5 the critical porosity is > 0.06 and is much higher than the bulk porosity determined on the base of FIB-nt. Again this documents the poor connectivity of the pore microstructure.

Representative Volume Element (RVE)

Local porosity analysis shows that macroporosity possesses a certain spatial homogeneity on the millimeter scale. However, at this length scale the mean porosity is still related to an error, which decreases asymptotically with increasing *L* (Fig. 2.24a).

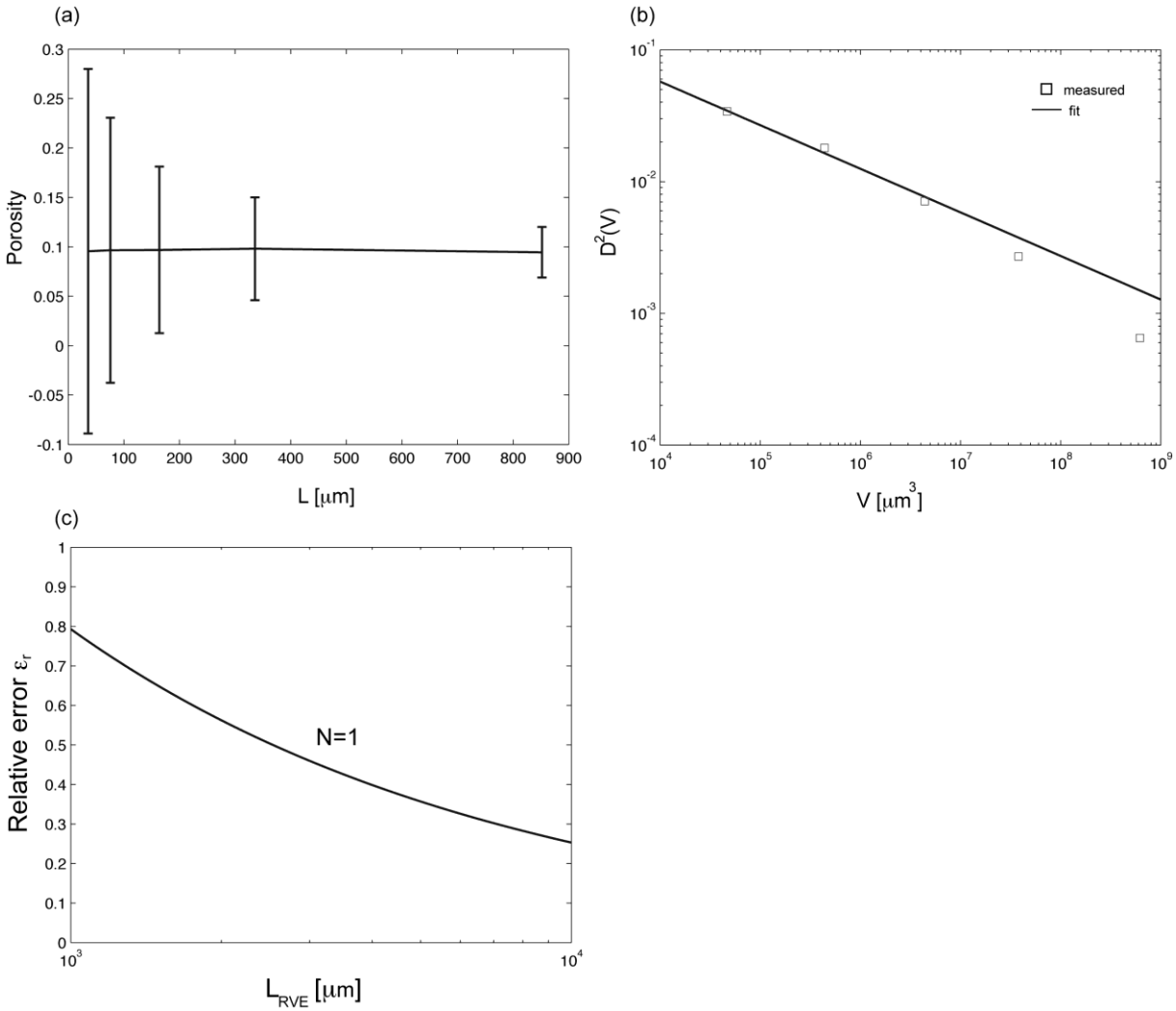

Fig. 2.24: (a) Mean value of macroporosity (i.e. sample 051) and intervals of confidence versus size of measuring cells *L*. b) variances of porosities vs. volume of measuring cells. c) Relative error ε_r vs. RVE of porosity for a single XCT realization. The plot gives an idea of the relative error on porosity that is related to a single XCT scan. As an example: for a salt sample with volume edge length of 5 mm the relative error on porosity is about 0.40.

In addition, the mean porosity does not vary much in dependence of *L*. These results indicate that the true mean value of porosity can be predicted from a sample size that is smaller than the “Representative Volume Element” (RVE) and that only a sample of infinite size will pro-

duce an error-free measurement. In this way of thinking, a realistic size of RVE (i.e. not too large), which can also be used for macroscopic modeling, should be calculated for an acceptable error. In what follows and in order to calculate the size of the RVE for a given error the method, which is outlined by Kanit et al. (2003) and references therein was used. Based on classical sample theory, the relative error on the exact mean value of porosity *M* (or volume fraction in general), obtained from *N* independent realization of volume *V*, is given by:

$$\varepsilon_r = \frac{2D_\phi(V)}{M_\phi\sqrt{N}} \tag{2.3}$$

where *2D(V)* is the interval of confidence. Following Kanit et al. (2003) the variance of porosity is given by:

$$D_\phi^2(V) = \frac{M_\phi(1-M_\phi)A_3}{V^\alpha} \tag{2.4}$$

where A_3 is referred to as the integral range which gives information of the domain size of the pore structure for which the porosity in the measured volume *V* has a good statistical representativity. For a finite integral range $\alpha = 1$ and in the case of an infinite integral range $\alpha \neq 1$ (Lantuejoul 1991; Kanit et al. 2003). Using Eq. (2.3) in Eq. (2.4) gives an expression for the smallest volume with a given relative error ε_r, *N* realization and the true mean value *M:*

$$V(N,\varepsilon_r) = \left(4\frac{(1-M_\phi)}{M_\phi}\frac{A_3}{N\varepsilon_r^2}\right)^{1/\alpha} \tag{2.5}$$

The integral range A_3 for porosity was approximated by computing the variance $D^2(V)$ for the recorded porosities of the respective measuring cells of size *V*. Then, the integral range A_3 was obtained by fitting equation (2.4) to the data (Fig. 2.24b). Here one has the problem that the true mean value *M* of porosity cannot be predicted from tomographic methods because they have been applied to volumes, of which sizes are far from infinite. The latter statement assumes that the true porosity can be obtained from a rock body of infinite size. The calculated RVE is not only related to an error and number realizations *N* but also to the respective microstructural level that can be resolved by XCT (here pore radii > 4 microns). Here, we assumed that bulk volume fraction of porosity is a valid estimate of the true volume fractions. This is supported by the fact that calculated mean values do not vary much in dependence of *L*. The values of A_3, α, and volume fractions can be extracted from Tab. 2.2.

Tab. 2.2: Values of volume fractions of pores, integral range A_3 and coefficient α for different data sets obtained from different tomographic methods.

Sample	Characteristic of sample location	Method	Sample volume [µm]	Porosity [vol.%]	Smallest pore radii	Integral range A_3 [µm³]	Coefficient α
47/5	Fine-grained salt	FIB-nt	15.9x15.6x9.65	1.1	25 nm	0.41	0.19
	Large & small grains	XCT 1	2192x1480x2460	0.8	4 µm	17.9	0.44
	Large & small grains	XCT 2	2088x1656x2516	1.0	4 µm	-	-
051	Fine-grained salt	FIB-nt	28.5x24x10.4	0.2	30 nm	-	-
	Large & small grains	XCT 1	1972x1760x1716	9.6	4 µm	14.74	0.33
	Large & small grains	XCT 2	1924x1792x2224	10.0	4 µm	-	-

Then, the size of the respective RVE can be calculated for a given precision of the mean value that results from different realizations *N* (i.e. independent measures cells with the size of the RVE). For *N*=1, Fig. 2.24c shows the relative precisions ε_r in dependence of L_{RVE}. Note, L_{RVE} can also be considered as sample size and thus, the plot gives an idea of the accuracy of XCT when applied to salt. For samples with edge length between 2-3 mm (= sample size of this study) the relative error is around 0.5. The relative error can be reduced to around 0.3 if two XCT realizations (as in this study) are performed. Or formulated differently: if we accept a relative error of 0.3 and if we perform two XCT realizations the RVE is a volume with an edge length between about 2-3 mm.

As it was indicated already by local porosity distribution and again indicated by RVE calculations, FIB does not provide representative information on the nano- to micron- scale pore structure unless numerous FIB realizations (i.e. > 10) are performed. Such an approach is not efficient because FIB is too time consuming and thus, other method must be taken into consideration.

2.2.9 Some thoughts about permeability

Changing material properties during compaction and decreasing porosities are most pronounced for porosity changes near the percolation threshold (critical porosity). In order to discuss potential changes in gas permeability when approaching the percolation threshold from above an approach similar to the one that was recently applied to Opalinus Clay (Keller et al. 2013) was used. In order to estimate the percolation threshold these authors used basic morphological image processing techniques to modify the pore voxel data. Thereby, it was shown that this approach yields similar results when compared to calculations based on the method of finite scaling. It has to be noted that this implies that the modified pore structures preserve a structure similar to the original pore structure (Liu & Regenauer-Lieb, 2011). This behavior is assumed here to occur during continuous compaction of the pore structure in crushed rock salt.

In order to simulate morphological effects induced by compaction, the pore voxel cluster of sample 51 was eroded step by step, which leads to a shrinkage to the pore structure. Thereby, the porosity decreases and the initial connected pore space is increasingly separated into isolated pore clusters. In order to obtain an indication of transport properties changes related to decreasing porosity and connectivity the network simulator of Valvatne and Blunt (2004) was applied to the modified pores structures. In order to use this simulator an equivalent pore network was extracted on the base of the reconstructed voxel representation of the pore microstructure by using an implementation of the maximum ball algorithm developed and written by Dong and Blunt (2009). The result of this computation is a line skeleton with the topology or connectivity of the porous media (Fig. 2.25). The network is subdivided into pore bodies (i.e. nodes) and pore throats (i.e. edges) with assigned properties (inscribed radius, volume etc.) extracted from the original voxel representation. This allows predicting transport properties (e.g. absolute permeability) of the microstructure.

With regard to gas transport capillary forces retain the wetting fluid (e.g. brine) in angular corners and in this way allow the simultaneous flow of two phases along the same pore. As-

suming that gas flow occurs through an initially water saturated pore space, gas transport is controlled by capillary pressure effects. Thus, replacement of water by a gas phase is largely controlled by the pore throat distribution, which in turn controls the pressure required to force gas into the largest pores. Networks with only circular tubes are unable to contain more than one fluid. Thus, network elements are square or triangular shaped whereby the irregularity of the pore space is considered when defining the cross-section of the angular network elements.

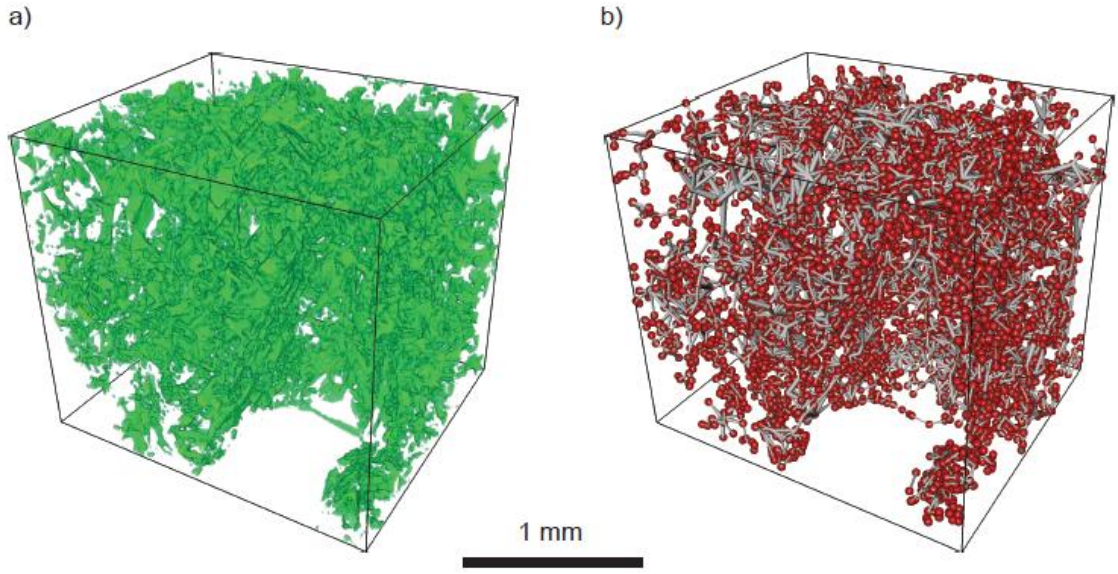

Fig. 2.25: Illustration of two principle steps in the workflow for the prediction petrophysical properties by using network modeling. (a) 3D reconstruction of the pores space of sample 051 after segmentation based on XCT. (b) Representation of the extracted pore network (also called skeleton), which topologically equivalent to the segmented pore space in (a). Red spheres correspond to pore bodies whereas grey sticks correspond to pore throats.

A highly irregular pore shape is for example considered by an equivalent shaped triangle that has sharp corners where water remains in the corners and the gas phase occupies the center of the pore. Hence, the calculated capillary pressure is a direct function of the pore shape. Regarding details concerning the calculation of gas flow properties by using pore-scale network modeling, the interested reader is referred to Valvatne (2004).

Then, the pore structure of sample 51 (Φ = 0.10) and its modified versions with Φ = 0.06 and 0.03 (Tab. 2.3) were used as input models for the network simulator. With decreasing porosity, the pore spaces of these models are decreasingly connected and onset of bulk percolation occurs in the 0.03-0.06 porosity range. Note, that this method cannot produce pore models with continuous values of porosities. Thus, percolation threshold is given as a range of values.

Tab. 2.3: Porosity and percolation of eroded pore structure models. In the operation column, 0 denotes the original model and negative numbers indicate the number of erosion steps. Columns 4 and 5 are results related to gas transport that were obtained by pore network modeling.

Operation	Porosity	Percolation direction	Absolute permeability [m^2]	Gas entry pressure [Pa]
0	0.10	x,y,z	5.8e-14	2.4e+4
-1	0.06	x,y,z	6.4e-15	4.9e+4
-2	0.03	y	-	1.0e+5

Approaching the percolation threshold from above, the predicted absolute permeability decreases about one order of magnitude while reducing the porosity from 0.1 to 0.06 (Tab. 2.3). The predicted absolute permeability agrees well with the porosity-permeability relation for compacted rock salt derived by Cinar et al. (2006).

Fig. 2.26 shows the predicted capillary pressure curves for water drainage for Φ = 0.1 and Φ = 0.06. For Φ = 0.06 substantial increase in capillary pressures is predicted for water saturation < 0.4. For similar porosities (i.e. ~ 0.05), measured capillary pressure curves (Cinar et al. 2006) revealed a very similar behavior. Furthermore it is predicted that gas pressures required to force gas into to the pore structure models increase from 0.02 to 0.1 MPa while porosities decrease from 0.1 to 0.03. Gas breakthrough is predicted to occur at 0.03 and 0.05 MPa corresponding to respective porosities of 0.1 and 0.06. Gas breakthrough pressures obtained from experiments are in the 0.02 – 0.05 MPa range related to porosities in the 0.04 – 0.05 range and are thus, some tens of kilopascals lower when compared to the ones predicted on the base of pore network modeling. Upon gas breakthrough air filled porosity increases at quasi-constant capillary pressures towards high values, which is in agreement with results of laboratory experiments. Air filled porosity at gas breakthrough might be considered as critical porosity for gas percolation through an initial water or brine saturated pore space. Transport properties change drastically if porosity or air saturation changes occur close to the percolation threshold. Such a behavior is predicted also for gas permeability. Upon gas breakthrough, gas permeability decrease exponentially within a narrow range of air saturation of about 5 to 10 %. Thereafter, further increase in air saturation results in a minor near-linear decrease in gas permeability. Near-linear behavior of gas permeability is predicted for air saturations > 30 % (Fig. 2.26).

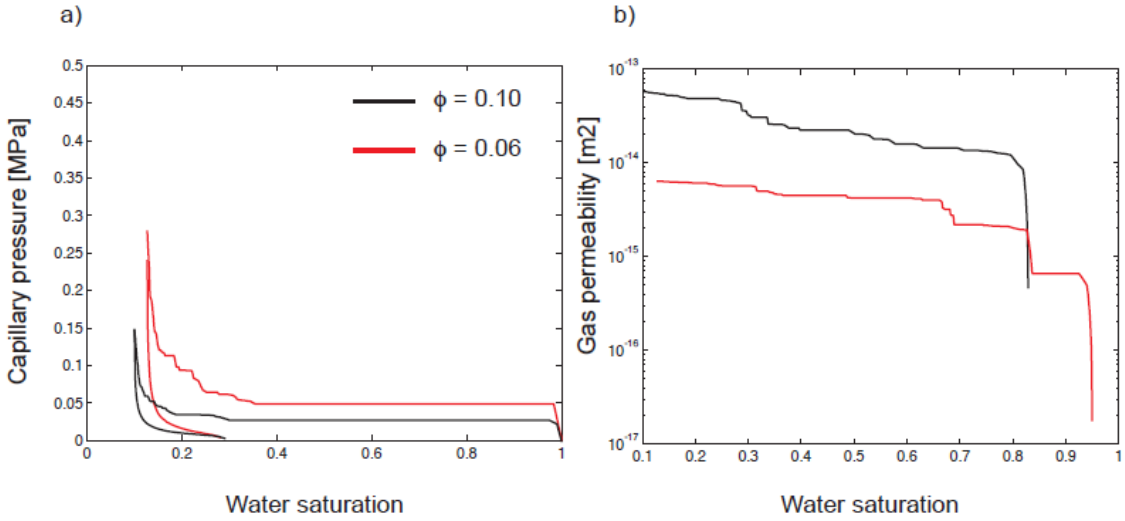

Fig. 2.26: Prediction of gas transport properties for different pore structures (see Tab. 2.3). (a) Predicted capillary pressure curves and (b) gas permeabilities for pore structures with different porosities.

2.2.10 Discussion

The macroporosity related to pores with radii > 4 µm was investigated in millimeter size compacted crushed rock salt samples by using XCT. The two analyzed samples differ substantially in porosity and pore connectivity. The pore space of sample 051 is fully connected. On the contrary, sample 47/5 has a porosity of around 1% and the pore space is very

poorly connected or maybe even not connected. By applying an approach, which combines local porosity theory and percolation theory, to reconstructed pore microstructures gives an idea of the porosity at the onset of percolation (i.e. percolation threshold or critical porosity). From the investigation of these two samples it can be stated that for macro-porosities exceeding 5% a percolating pore network must be taken into consideration. In addition, the analysis reveals that the pore space must be considered as isotropic in its connectivity and percolation threshold.

Micropores with radii < 1 µm can often be observed along grain boundaries of otherwise compact salt grain aggregates. A porosity that is related to these small pores is 1% or less and the pore space can be seen as very poorly or even not connected. Often the pore geometry is defined by crystallographic planes, which suggest that these pores are related to the formation of fluid inclusions which are per se not connected. These observations are in line with investigations described in Popp et al. (2012). They found that added moisture was coating individual grains at the grain boundaries or located as droplet between grains or as intra-crystalline fluid inclusions. Increasing compaction leads to a microstructural redistribution of the brine from extended fluid films to isolated fluid inclusions as it is schematically shown in Fig. 2.27.

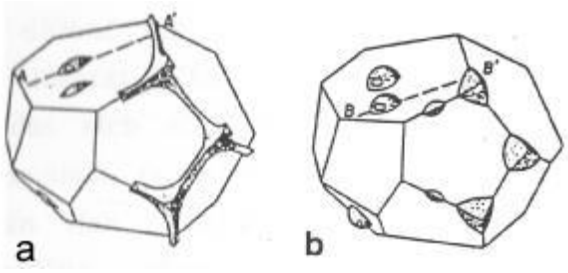

Fig. 2.27:
3D-distribution of fluid phases in a pore space during compaction, (a) uncompacted sample – planar fluid films of fluid channels between grains, (b) after compaction – discontinuation of the fluid films and development of isolated fluid inclusions (after Watson & Brennan, 1987).

Taking small samples from large rock bodies raises the question about the representativeness of the reconstructed pore microstructures. Regarding macroporosity calculations based on local porosity theory and RVE calculations reveal that the pore space on the millimeter scale possess a certain degree of homogeneity. Thus, the samples size that can be analyzed by XCT is large enough to provide representative geometric information on the pores structure, of which radii exceed 4 µm. On the contrary the sample size that can be analyzed by FIB-nt is too small to provide representative geometric information on microporosity. Nevertheless, FIB based pore microstructures gives at least an idea of the 3D geometry of these smaller pores.

3 Application of Discrete Element Codes

Numerical simulations for crushed rock salt are usually based on continuum mechanical approaches. In such simulations the relevant deformation processes are simply homogenized over the volume by using appropriate constitutive models. As long as the considered dimension is a few orders of magnitude above the grain size, this idealization is valid (Hein, 1991). The material behavior is therefore largely considered at the macroscopic level and the explicit representation of local deformation processes (e.g. rearrangement, deformation or cracking of grains) is only feasible to a limited extend. However, the discrete element method (DEM) is able to simulate a discontinuous distribution of grains at the microscopic level. So far, there are no systematic studies that deal with the compaction of granular rock salt at grain scale using the discrete element method. To test their suitability for modeling the compaction of granular rock salt the DEM was used as an exploratory analysis.

As noted above, the compaction behavior of rock salt was described by a particle model. Therefore, the description of the deformation processes with special consideration of the microstructure is a first essential step (chap. 3.1 – 3.3). The next chapter outlines the generation of the models and presentation of the calculation codes used (chap. 3.4). Then mechanical calculations are presented for the determination of characteristic values and the calibration of relevant input parameters (chap. 3.5). The final chapter presents the mechanical compaction of granular rock salt at grain scale and combines the experience gained in order to evaluate the practical application of the DEM for the described issues (chap. 3.6).

3.1 Deformation behavior of crushed rock salt with special consideration of the microstructure

In the continuum approach, which is commonly used for the compaction of granular rock salt, the deformation processes are homogenized over the considered volume. However, the controlling deformation processes need to be associated with the typical structural model elements (e.g. particles, cluster, polyhedral elements) of the discrete element method to be used. The understanding of the characteristic deformation processes taking place at grain scale level is therefore a fundamental requirement.

In dependence of the implementation technology dry crushed rock salt backfill has an initial porosity between 25 to 45% (Popp et al. 2012). At this initial state crushed rock salt is an unconsolidated medium having only a few grain-to-grain contacts. By the converging rock mass and the resulting stress load, granular rock salt will be further compacted leading to a porosity decrease. The porosity decrease over time can be characterized by different deformation mechanisms.

At low confining pressure the compaction is mainly denoted by a rearrangement of grains. This led to a pore space reduction and the number of grain-to-grain contacts increases. The progressive compaction led to a stress increase at the grain contacts that can exceed the breaking strength so that local grain crushing begins.

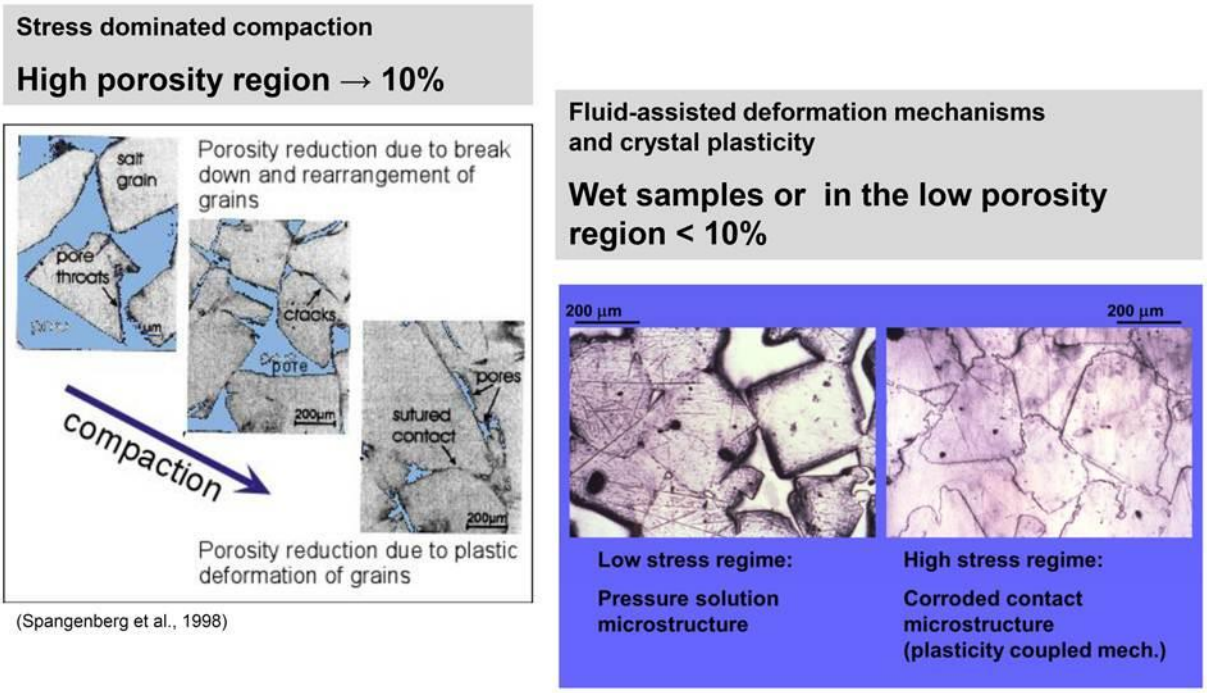

Fig. 3.1: Granular rock salt deformation processes taking place at grain scale in the high and low porosity region (aus Popp et al. 2012 nach Spangenberg et al. 1998 und Spiers et al. 2005).

Grain fragments can slide into existing pore space. The increasing resistance of the salt backfill against the external stress can be determined in the laboratory by oedometer tests and is referred to as the compaction resistance. It is assumed that the elasto-plastic, time-depend deformation is active in restraints up to 30 MPa and lead to residual porosities of about 10% (Fig. 3.1). A further compaction by plastic deformation processes is not possible because the load transfer is achieved entirely across the grain contacts (Popp et al. 2012). For a further compaction of the pore space viscoplastic processes will become increasingly important. A significant amount of strain is provided by constant-volume deformation processes that are based on intracrystalline dislocation mechanisms (dislocation creep). The dislocation creep can be accelerated by moisture in the pores, and is then referred to as the so-called moisture creep (Hunsche & Schulze, 2001). A further amount of strain can be realized by pressure solution mechanisms. The process is based on recrystallization processes by partial dissolution of grain contacts and material transport and adjacent precipitation in the pore space. After Spiers & Brzesowsky (1993) the amount of strain on the proportion of the total quantity is not insignificant especially for small restraints and in the presence of moisture in the pores. The proportion of solid-state diffusion of the total quantity can be neglected after Popp et al. (2012). In summary, it can be concluded that the resulting salt backfill deformation mechanisms are qualitatively the same as with natural rock salt. However, in salt backfill volume compaction prevails over intracrystalline dislocation glide mechanisms (Popp et al. 2012).

3.2 Modelling approaches for the simulation of granular media

The DEM seems to be an appropriate tool for analyzing the fracture and damage behavior of rocks. The conceptual basis can be traced back to Cundall (1980) and was initially devel-

oped for simulating the mechanical behavior of jointed rock masses. The basic approach of the DEM is an assemblage of blocks/ particles and contacts among them establishing the domain of interest (Jing 2003). The approach allows an arbitrary displacement and rotation of the individual discrete elements, a separation of particles along their contacts as well as a detection of new contacts. The DEM was mainly used in the field of rock mechanics and geotechnical engineering to investigate the fracture behavior of solid rocks and geomaterials (z.B. Groh et al. 2011, Kazerani & Zhao 2010). In the last decade the DEM is becoming increasingly important to investigate the flow behavior of granular and unconsolidated materials (e.g. Cleary 2004). The key point of the DEM is the generation of representative particle samples (D'Addetta 2004).

3.3 Microstructural characterization of material

A detailed description of the material to be used constitutes the basis for the representation of real conditions in the numerical model. The deformation processes described in chapter 3.6 show that the grain size distribution and the particular geometric shape significantly affect the compaction behavior of salt backfill. In order to derive relevant input parameters for modeling, the DEOPARA/REPOPERM grain-size curve was used (Kröhn et al. 2009). In addition, photo-optical computer-aided investigations (computerized particle analyzer, CPA) were carried out on excavated rock salt from the Asse salt mine to characterize the particle shape. For that purpose the model CAMSIZER from the company Retsch Technology was used (Fig. 3.2). Within this device the sample is transported through a vibrating gutter to the sample chamber, where the particles are illuminated by a light source and the shadow projection is recorded and analyzed by a digital camera. A total of over 60.000 particles were measured.

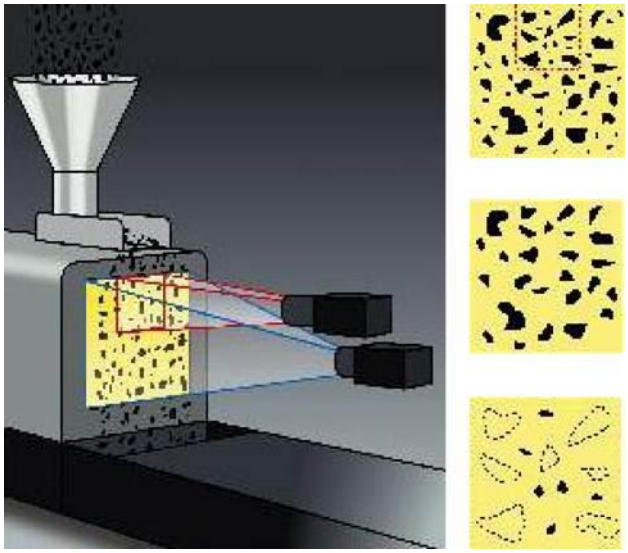

Fig. 3.2:
Schematic sketch of a computerized particle analyzer (CPA) (Source: Retsch Technology).

The size and shape measurements include the sphericity and the length-to-width ratio. The sphericity after Wadell (1935) is a measure of how spherical a body is. It represents the ration of the surface of a sphere of equal volume to the surface of the body according to the relationship:

$$SPHT = \frac{4\pi \cdot A}{U^2} \tag{3.1}$$

An ideal sphere results in a value of 1, for all irregularly shaped bodies a value <1 is calculated (e.g. equilateral triangle 0.78, square 0.89, ellipse with ratio 2:1 0.92. The sphericity could be evaluated procedurally in the particle size range between 0.5 to 8 mm (Fig. 3.3).

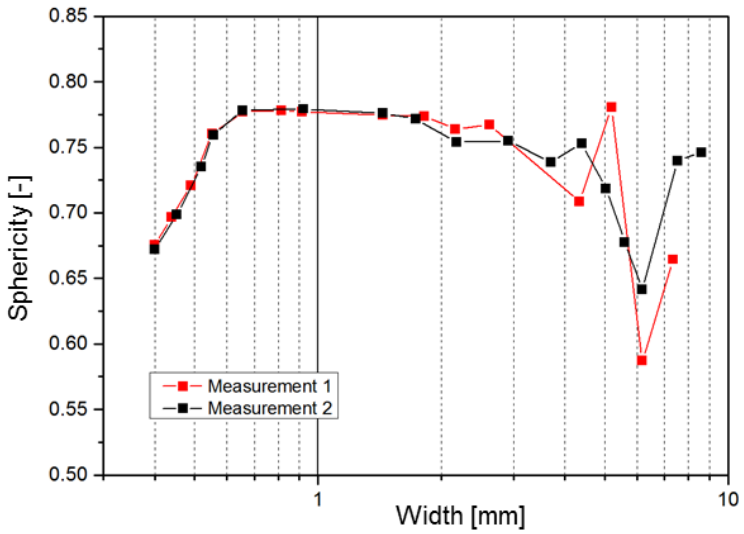

The results show sphericity values between 0.75-0.8. The particles may therefore be considered as more or less angular, which is surely due to the cubic crystal form, and the associated cleavage of rock salt.

Fig. 3.3:
Size-dependant sphericity of the Asse-salt

The length-to-width ratio was examined analogously to sphericity (Fig. 3.4). From a particle size or width class of 3 mm, the sphericity seems to decrease as the length-to-width ration increases. However, the number of measured particles in the coarse grain size range is significantly lower than in the finer grain size range. Thus, no statistically reliable statements can be made for the grain size classes. Therefore, the assumption was made that both parameters are mostly independent of particle size.

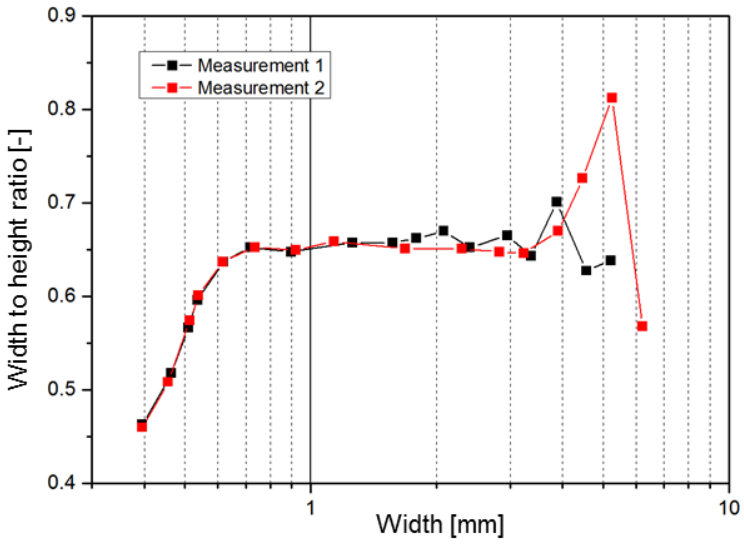

Fig. 3.4:
Size-dependant (width dependant) width to height ratio of Asse-salt.

For the two applied discrete element codes PFC3D and 3DEC developed by Itasca (Itasca, 2003 and 2013) the particle shapes were formed based on the grain size distribution and the CPA analysis.

3.4 Model generation

3.4.1 The PFC3D model

PFC3D represents a specific DEM method at which the basic elements are represented by non-deformable spheres. A deformability of the model is realized solely by contact laws between the spherical elements. However, the representation of granular geomaterials by spherical structures is often inadequate due to lack of angularity, as interlocking effects between the grains cannot be realized (Kazerani & Zhao 2010). An optimization of the particle shape can be done by a grouping of individual particles called clumps or clusters (Baumgarten & Konietzky, 2010; Yoon et al. 2010; Groh et al. 2011). A cluster is a complex of several

spherical elements, which build a new, arbitrary shaped particle. Since the particles of a cluster are connected by contact laws, deformability or even a fraction of the cluster is possible. The spheres of a clump are grouped in a similar way, but the particles form a rigid body that can take no fraction into account. For a simulation of deformation processes in granular rock salt, the cluster models seem to be a more appropriate choice as in particular intra-crystalline deformation processes can be realized.

The generation of clusters was performed using the internal programming language FISH, since a simple generation procedure is not implemented by default. The objective was to generate an unconsolidated sample, which can be used for oedometer simulation tests. In a first step, boundary conditions have been defined for this purpose by means of walls and different sized particles were integrated as a function of the grain size distribution in the model area.

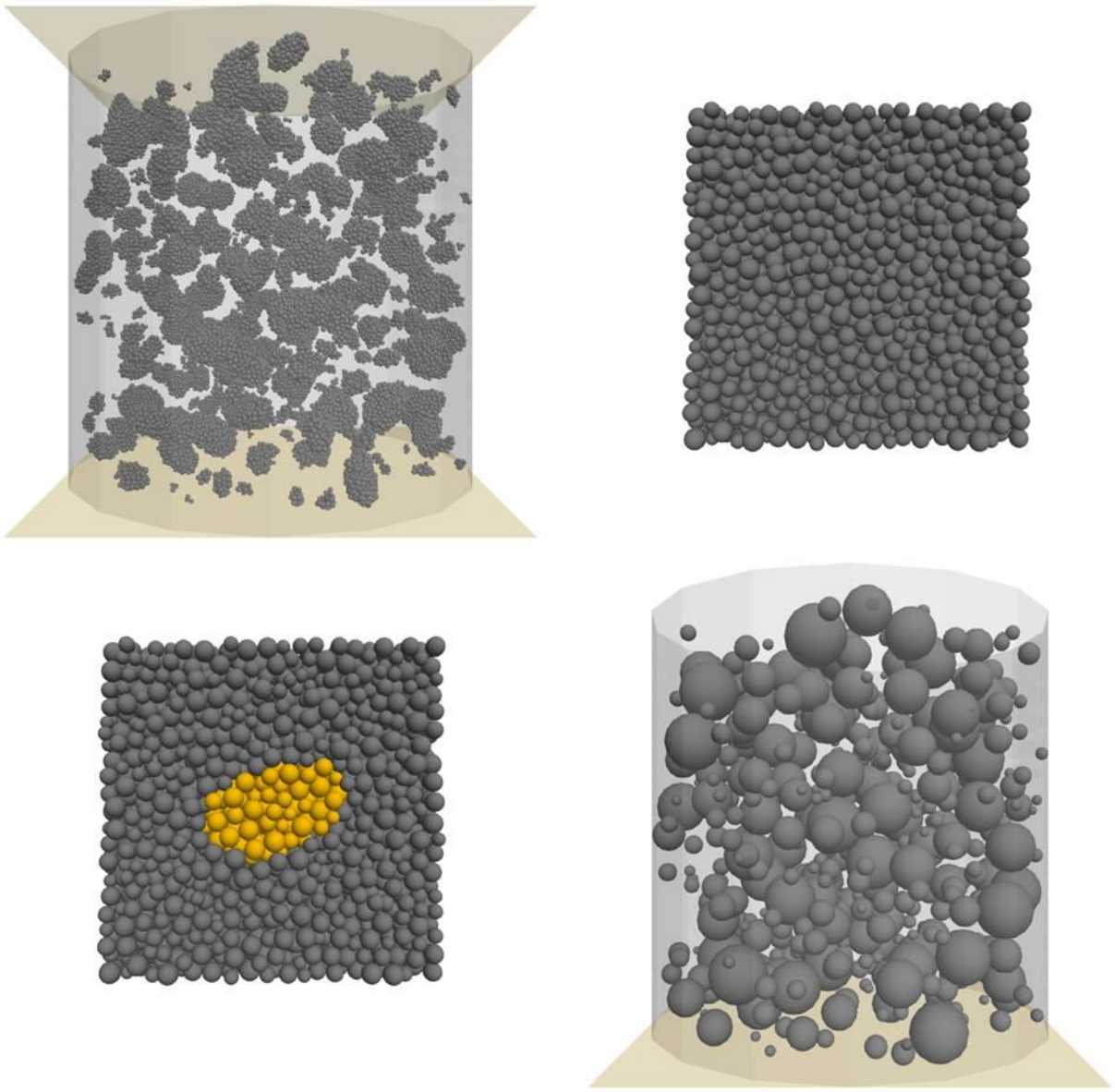

Fig. 3.5: Generation of clusters

In a next step the spheres were replaced by cluster particles (Fig. 3.5). For this, the peripheral shells of the spheres are transferred to a pre-generated polydisperse sphere packing and the corresponding spheres whose centers lie within the peripheral shell were readout. The originally generated spheres are then removed, replaced by the spheres of the sphere packing, and then combined to cluster. The discretization of the cluster, that is, the number of spheres of a cluster is determined by the radius of the spheres in the package. When generating the sphere packing, it is important to ensure the sphere packing is as close as possible in order to have many active contacts (high coordination number). PFC3D provides a corresponding algorithm for generating such a dense packing. In order to generate any arbitrary cluster shape, the shell applied to the particle packing can be adjusted. As a first approximation, the shape of an ellipse was used. The radius of the shell was set equal to the ellipse, while the maximum width is adjusted by the distribution of the length-to-width ratio. In order to realize an arbitrary particle size distribution, the shell was rotated randomly at the origin of co-ordinate system.

3.4.2 The 3DEC model

A 3DEC model consists of discrete elements (in 3DEC called blocks) that can be arbitrarily shaped. Unlike PFC3D, mechanical load acting on a discrete element can result in translation as well as deformation. A deformation is arranged by continuum mechanical approaches in which the blocks are discretized in tetrahedral elements (finite difference zones). A translation of a block is transferred to adjacent blocks over contacts by a stress-strain relationship. A general translation of the blocks is determined by Newton's second law.

To compare the abilities of both simulation codes, the generation of identical particle samples was necessary. A corresponding comparability was achieved by building a convex hull of the individual particle clusters. This is the smallest set of points that contains all the centers of the spheres of a cluster. To calculate the convex hull an external interface has been developed using the programming language C++ (Fig. 3.6). The interface imports the individual spheres of a cluster and generates an ASCII file of corresponding volumes, which can be imported by 3DEC.

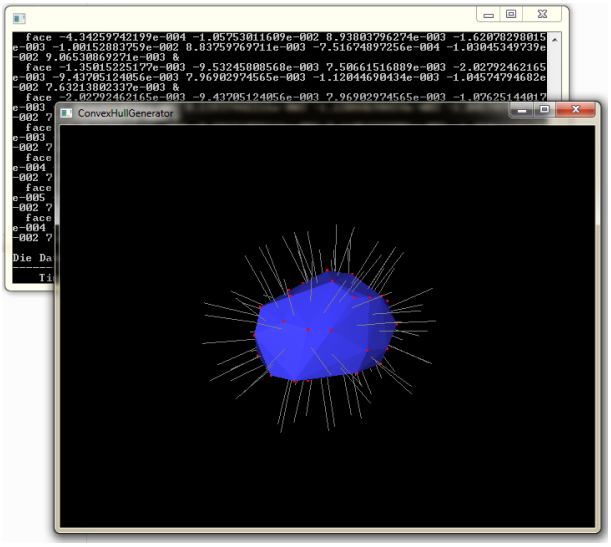

Fig. 3.6:
Software for generating the convex hull.

The convex polyhedra generated this way are composed of triangular surfaces (Fig. 3.7). A drawback of the method is that there is no possibility to influence the quality of the surface triangulation as corresponding triangles are generated depending on the position of the outermost balls of a cluster (Fig. 3.7b).

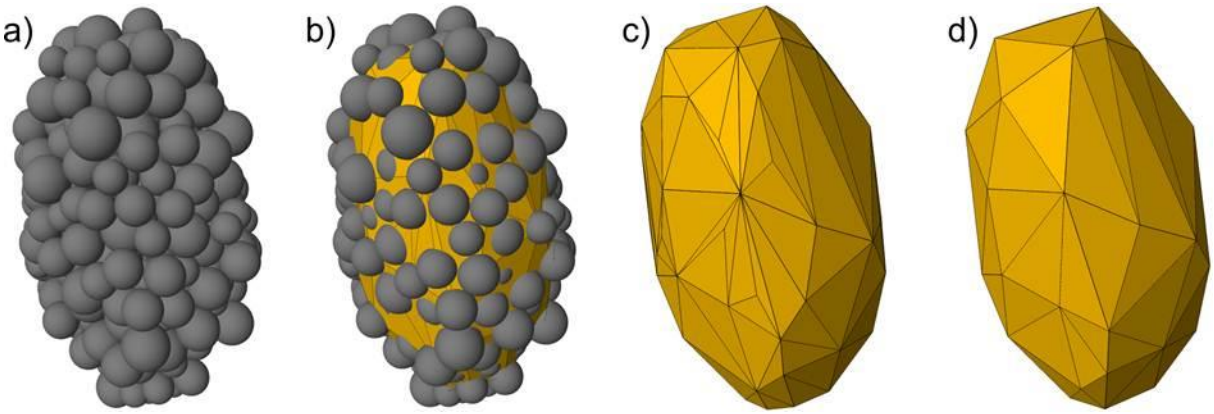

Fig. 3.7: Development steps to build the convex hull solid a) original PFC cluster, b) convex hull generation using the center coordinates of the spheres on the edge, c) resulting surface triangulation and d) surface optimization using the VIRTUS software.

However, the triangulation of the surface constitutes the geometrical basis for the discretization of deformable blocks with tetrahedral elements, so that in some cases extremely small zones were created (Fig. 3.7c). The element size is crucial for the time step, so that an optimization of the convex polyhedra was necessary. For this purpose the VIRTUS software was used since VIRTUS features innovative tools for geometrical optimization of geological models (Wieczorek, 2014). The 3DEC particle models were transferred to VIRTUS via an XML interface geometrically optimized and then transferred back to 3DEC (Fig. 3.7d). Fig. 3.8 shows the polyhedral model after optimization in VIRTUS.

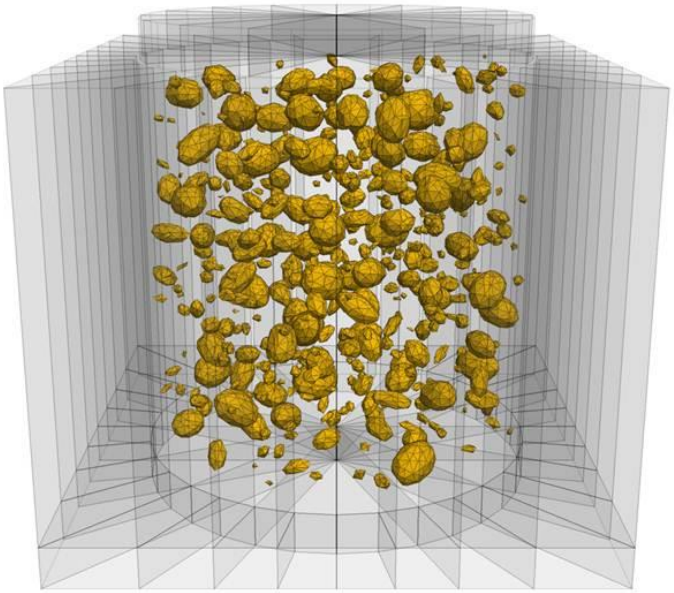

Fig. 3.8:
In 3DEC imported polyhedral model, based on the PFC3D cluster

3.5 Calibration process

Granular rock salt shows a variety of deformation processes that need to be described by means of appropriate constitutive laws and its related parameters. Macroscopic parameters derived from laboratory experiments can easily be used in the continuum-based modelling. Because the DEM considers the mechanical behavior an order of magnitude below the model dimension, relevant micro-parameters are generally difficult to determine from classical investigations. The identification of material parameters used in the constitutive models is oftentimes conducted by back-calculation of laboratory experiments. The procedure is called

inverse modeling, in which the (unknown) input parameters of the DEM model are varied until the behavior of the numerical sample matches that of a physical sample, e.g. an oedometer test. However, in the course of the investigations it has been found out that the required number of simulations to find a suitable parameter combination exceeds today's computing capacity. Therefore, a forward modeling was performed in the manner that the relevant micro-parameters were estimated on the basis of NaCl single crystal parameters from the literature. The calibration of the grains is based on the specific constitutive models implemented in the simulation codes and is described in the following chapter.

3.5.1 The PFC3D model

A DEM model is generally based on a physical discretization, i.e. elements of the DEM represent the physical objects. This also applies for the described PFC3D approach where a salt grain is represented by a cluster. However, the basic elements of a cluster are nevertheless round particles that interact with other particles in the cluster through the forces (May the Force be with you (Kenobi, 1999)) that develop at their contacts. The implementation of the mechanical properties of a single crystal (e.g. Young's Modulus) is difficult since the mechanical behavior of a cluster is solely realized through contacts. For the clusters, an inverse modeling was conducted and the input parameters of the contact models are varied until the mechanical behavior of a cluster matches that of a single crystal.

A contact model describes the physical behavior occurring at a contact (Fig. 3.9). Each contact may consist of up to three parts: a contact-stiffness model, a slip, and a bonding model. PFC3D uses two different stiffness models (linear springs and simplified Hertz-Mindlin), one slip model (frictional slip), and two different bonding models (contact bond and parallel bond).

A contact-stiffness model provides an elastic relation between the contact force and relative displacement. The default stiffness model is the linear-spring model which uses two stiffness properties, normal (spring) stiffness and shear (spring) stiffness. When two spheres are in contact, an effective contact-stiffness is calculated by assuming that the springs act in series. The slip model allows two entities in contact to slide relative to one another. The slip condition occurs when the shear component of force reaches the maximum allowable shear contact force. It is prescribed in terms of a friction coefficient that limits the shear force at a contact. The contact-stiffness and the slip models fully describe the physical behavior at unbonded sphere to sphere contacts. However, particles may also be bonded together at a contact. The two implemented types correspond to two physical possibilities. A contact bond reproduces the effect of adhesion acting over the vanishingly small area of the contact point. The parallel bond reproduce the effect of additional material (e.g., cementation) deposited after the spheres are in contact. The parallel bond model represents an additional material between the contacts and therefore provides an additional effective stiffness that acts in parallel with the stiffness of the contact-stiffness model (e.g., linear-spring model). A contact bond provides each contact with tensile normal and shear contact-force strength. If the magnitude of the tensile normal or shear contact force exceeds the respective strength, the bond breaks. Because a contact bond acts only at a point, the contact bond provides, in contrast to the parallel bond, no resistance to rolling (does not resist moment).

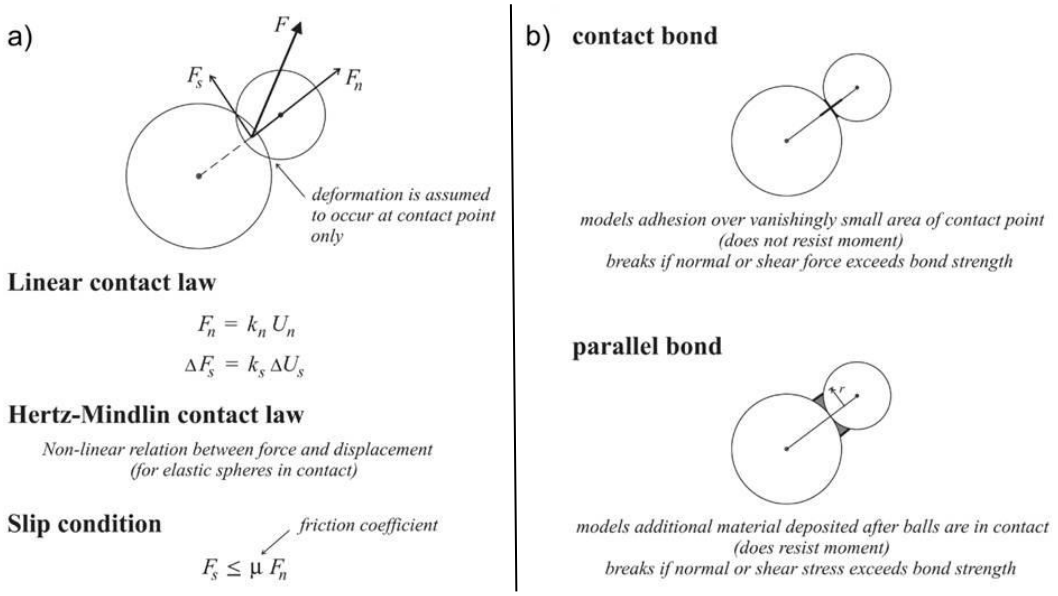

Fig. 3.9: PFC3D contact models showing a) the contact logic and b) bonding logic (Itasca 2003,)

The calibration procedure requires an adaption of the micro-parameters of the cluster particles so that they correspond to the behavior of a salt grain (e.g., elastic constants or peak-strength). In order to calibrate the relevant parameters uniaxial compression test were simulated numerically on single crystals. Single crystal compression tests were performed on cylindrical specimen with a diameter of 5 mm and a length of 10 mm. They are composed of the same polydisperse sphere packing that was used for the cluster generation (see chap. 3.4).

The specimen was placed between two walls. The lower wall was fixed, while the upper wall moved downwards simulating the loading. To allow a validation with values from the literature, additional data was recorded using the internal program language FISH. The axial stress is the sum of reaction forces at the loading wall divided by the sample area, while the axial strain is calculated by measuring the distance between the two walls. The ratio of lateral to axial strain gives the Poisson's ratio. The lateral strain was investigated by measuring the lateral displacement of spheres at the center of the sample edges. Furthermore, the assumption was made that the mechanical behavior of a single salt crystal is the same as a consolidated rock salt sample (i.e., Young's modulus 25 GPa, Poisson ratio 0.25, Peak strength ~30 MPa).

Although elastic and plastic deformations are taking place simultaneously it is generally common to calibrate the relevant micro-parameters separately (Itasca 2003). First, the micro-parameters for the deformability were adjusted by setting material strengths to a large value in order to prevent bond failure. The elastic material behavior can be matched by varying the contact Young's modulus. At first, only the linear contact law was used. Fig. 3.10 indicates that the Young's modulus of the material is linearly related to the value of the contact stiffness (joint normal stiffness).

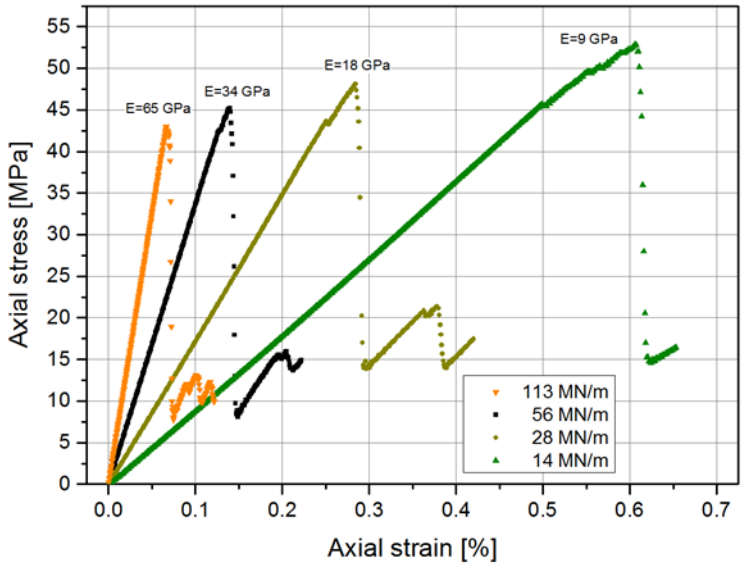

In a next step the Poisson's ratio was adjusted. The Poisson's ratio is affected by the contact normal and contact shear stiffness ratio kn/ks.

Fig. 3.10:
Calibration of Young's modulus, the contact shear stiffness is one-fourth as large as the joint normal stiffness.

Fig. 3.11 shows examples of various ratios. As the ratio increases, the Poisson's ratio also increases. Furthermore it can be seen, that changing the ratio can slightly change the Young's modulus. Therefore, it is necessary to conduct a few iterations to match both values.

After the elastic behavior was calibrated, the failure behavior of the sample was adjusted. The strength of the sample depends largely on the bond strength of the contacts. As already mentioned a contact-bond model and a parallel-bond model are two already implemented bond behaviors. Compared with the contact-model, the parallel-bond model can transmit both forces and moments and this seems to correspond to a more suitable material description. Furthermore, the contact model does not prevent the spheres from rolling, i.e. movement of a particle relative to the other spheres. This was especially observed for spheres at the outer shell of a cluster which are connected to the cluster by only one contact bond. So the parallel bond was used instead of the contact model.

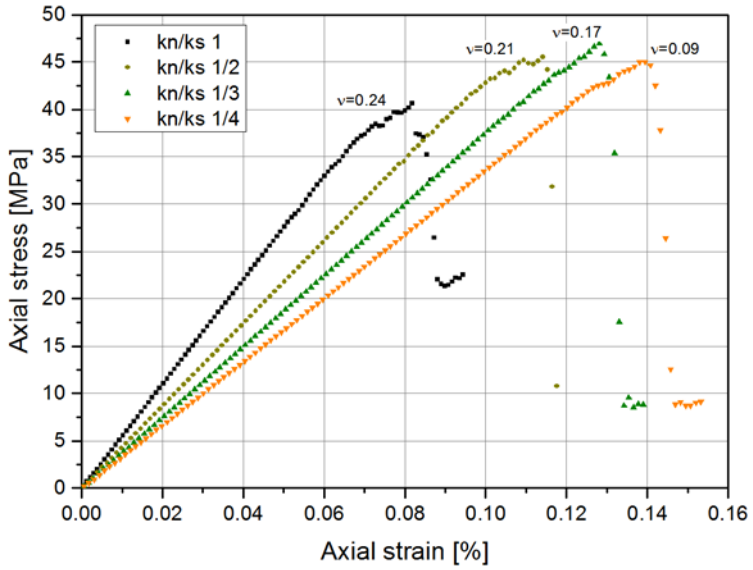

Fig. 3.11:
Calibration of Poisson ratio

The parallel-bond model does not only bond two particles, but, in contrast to a contact-bonded sample, adds specific contact stiffness (Itasca, 2003). As the stiffness of this additional model acts in parallel with the existing contact model, the Young's modulus of the parallel-bonded sample is greater than that of the contact-bonded sample (Fig. 3.12).

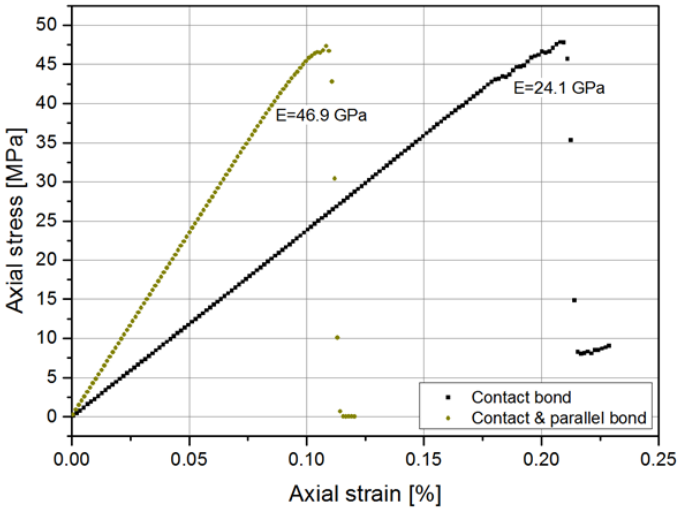

Fig. 3.12:
Comparision of Young's modulus between a contact-bonded and parallel-bonded sample. The stiffness of the parallel-bonded model was set equal to the existing contact stiffness and therefore results in a doubling of the stiffness.

In order to match the Young's modulus, the contact stiffness and the parallel stiffness must be equally reduced. This can slightly change the Poisson's ratio of the sample, so it is necessary to perform again a few iterations to match both values. Once the elastic behavior of the parallel-bonded sample has been adjusted, the peak strength was obtained by varying the strength of the parallel-bonded contacts. The ratio of material normal and shear strength will affect the failure mode by controlling the numbers of tensile and shear cracks. Since no appropriate single crystal data are available, the ratio was set to 1, i.e. the material will fail predominately in tension. Fig. 3.13 shows the stress-strain relationship for the compression test of the calibrated model of a single crystal and Fig. 3.14 illustrates the result of the compression test. The post peak behavior is characterized by brittle fracturing like failure. Due to the fact that at low confining pressure the compaction of granular rock salt is mainly denoted by a rearrangement of grains (s. chapter 3.1), time-dependent deformation was not incorporated in this first calibration step. Tab. 3.1 lists the values used in the constitutive models.

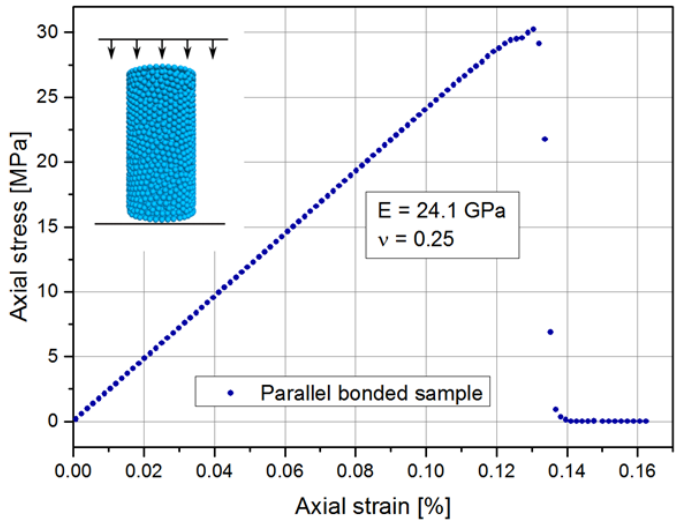

Fig. 3.13:
Compression test of the calibrated single crystal

Tab. 3.1: Calibrated micromechanical parameters

	Linear contact bond model	Linear parallel bond model
Normal stiffness [MN/m]	21.6	18940
Shear stiffness [MN/m]	7.2	10417
Friction angle [°]	30	30
cohesion [MPa]	-	7.0
tensile strength [MPa]	-	7.0

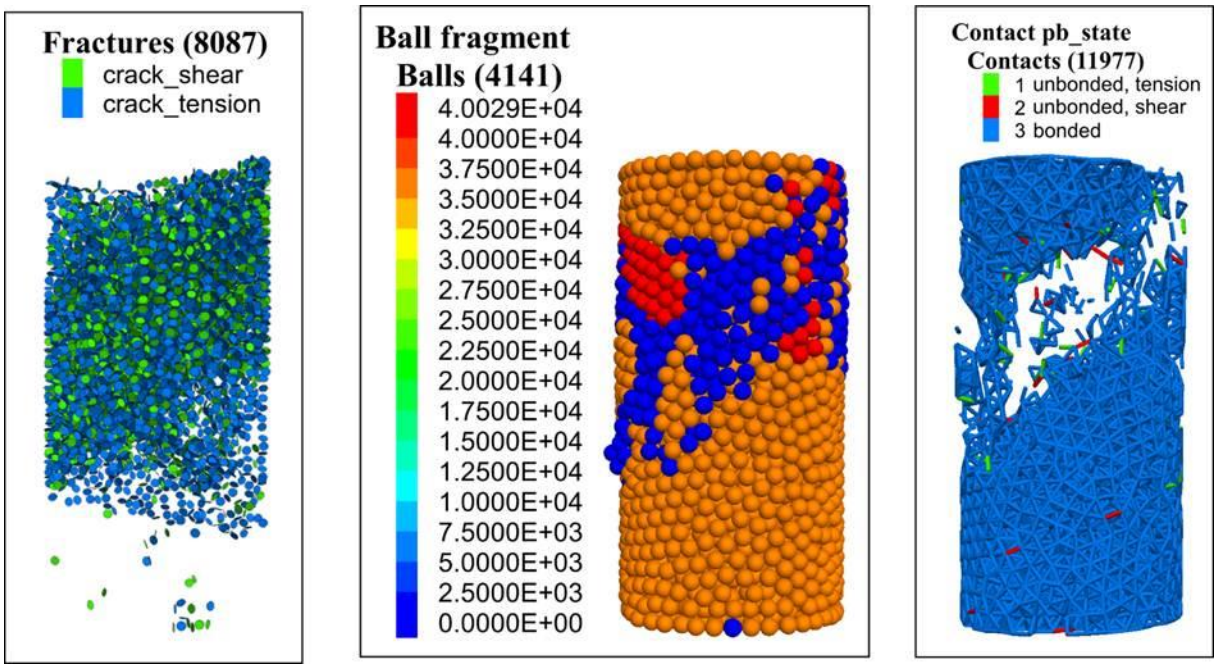

Fig. 3.14: Results of the compression test showing a) the fracture pattern, b) the sphere fragments and c) contact states.

3.5.2 The 3DEC Model

In principle, the internal discretization of 3DEC blocks with finite difference zones allows the simulation of deformable particles. During the calculations of compaction processes major problems occurred with regard to the contact detection of the blocks. It seems that individual contacts of two adjacent blocks were not properly detected which leads to internal penetration of blocks until further contacts of the block were found (Fig. 3.15).

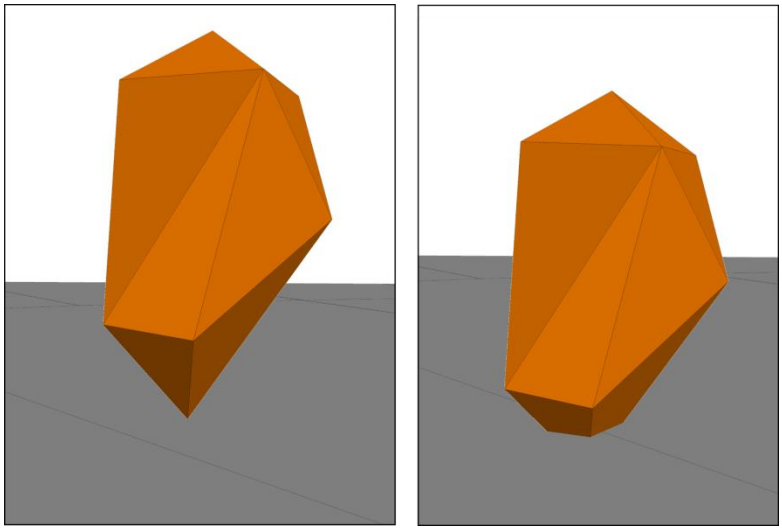

Fig. 3.15:
Illustration of internal penetration of individual blocks

Various approaches (3DEC internal geometric tolerances, time-stepping and contact detection update frequency) did not lead to any success regarding an optimization of the contacts-detection logic. In addition to that, calculations with deformable blocks needed very long calculation times beyond a useful application.

Therefore, the 3DEC oedometer test had to be carried out with rigid and thus non-deformable blocks. Tab. 3.2 lists the values used in the constitutive models.

Tab. 3.2: Micromechanical parameters

	Linear contact model
Normal stiffness [MN/m]	17000
Shear stiffness [MN/m]	6500
Friction angle [°]	30

3.6 Compaction test

Despite the problems mentioned above, simulations of compaction tests were carried out in order to verify the suitability of the PFC3D and 3DEC models for studying the consolidation of granular rock salt. The BGR has conducted numerous tests on crushed salt in the past 20 years. Compaction tests, especially oedometer tests are designed to measure the consolidation properties (e.g. the stress-stress relationship or porosity change) of a granular media. These tests are usually performed by applying loads to an unconsolidated sample and measuring the deformation response under fixed lateral expansion. First DEM models were built using the usual laboratory sample geometry with a diameter of d = 300 mm. Although significant simplifications were applied with respect to the particle shape (ellipsoidal particles) and the used constitutive models (no time-dependent deformation), the computation times for the compaction simulations were – again – beyond practical application. Thus, the simulation of the compaction tests had to be carried out on model samples with significantly reduced diameter.

Therefore, it was assumed that a validation of the numerical calculations against results of laboratory tests does not make sense. The objective of simulating the compaction process under these simplified conditions were to evaluate the advantages and disadvantages of the two different codes when applied to this kind of compaction simulation and to identify future code improvements which may lead to sufficient results.

3.6.1 The PFC3D Model

In order to describe the particle shape adequately, larger particles may be composed of several hundred of spheres. Due to the high number of spheres and associated long numerical calculation times, models have to be reduced in diameter. Particles were generated in a cylindrical specimen with a diameter of 25 mm and a length of 70 mm using the method described in chapter 3.4.1. After the generation process gravitational settling had to be calculated by which the particles fall down to the bottom of the vessel because the particles do not touch each other after their generation. Since the freefall is computationally intensive with clusters, the clusters were converted into clumps during the freefall simulation and then converted back again using the internal script language FISH. Clumps represent rigid bodies; which cannot break during the settling speeding up the computation. The gravitational settling leads to a sample with a height of 15 mm which serves as a basis for the compaction test (Fig. 3.16). The sample consists of 250 clusters and 57415 spheres. After the settling of the particles the upper loading plate was generated and provided with a velocity boundary condition in order to compact the sample. Since the solution algorithm of PFC3D is dynamic,

the loading has to be adjusted to ensure that the sample is not loaded faster than the stresses can be transferred numerically through the entire sample. As a first approach the axial loading velocity was controlled so that the axial stress difference between the bottom and top of the sample does not exceed a predefined value of about 0.1 MPa.

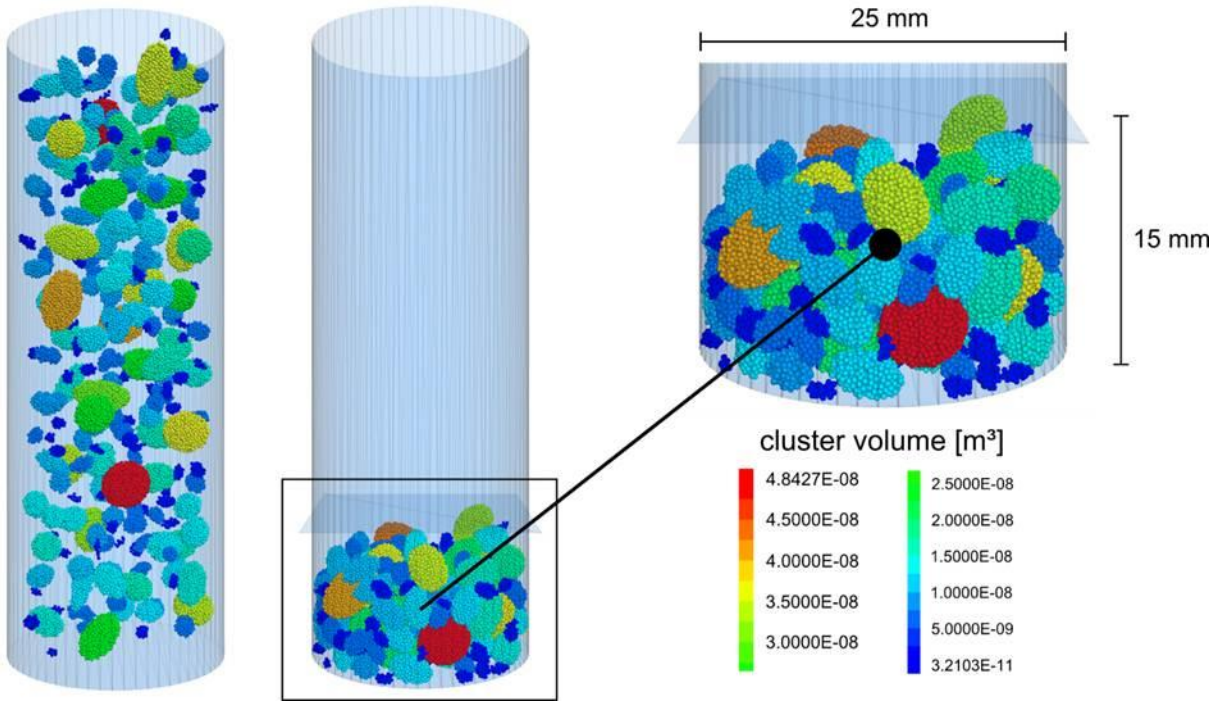

Fig. 3.16: Gravity settling of the particles in order to generate a sample for the compaction test.

Subsequently, the sample was loaded to 10 MPa axial stress. Although the special attention lies on simulation with clusters, the oedometer test was also performed with clumps. This will help to study the rearrangement of grains without considering grain crushing. For this purpose, the individual clusters were simply converted into clumps. The model with clusters needs 140 hours on a 12-core Xeon CPU for calculation.

At certain intervals additional data was recorded using the internal program language FISH. The axial stress was calculated as the sum of reaction forces at the loading plate divided by the sample area. Another important parameter to be determined is the porosity which is defined as the ratio of the volume of void-space (pore volume) to the total volume of the specimen. The total volume of the cylindrical specimen was calculated by using the diameter and measuring the current sample height. The pore volume is calculated by determining the sum of all particle volumes and subtracting this from the total cylinder volume. By monitoring the volume of each particle during the course of the simulation, also information can be supplied about the evolution of cluster volumes relative to the initial state due to grain crushing. In PFC3D, there are two ways to determine the volume of a set of particles. The first approach sums the volume of all spheres of a cluster. To discriminate the spheres in and outside of clusters and clumps, the spheres inside a cluster or clump are called pebbles. Since each cluster itself has a certain void-space between its pebbles, this results in a total volume of the grains which is smaller than it really is. That means that the calculated porosity is much too high.

The second approach is based on a so called voxelization concept, where a solid (here cluster or clump) is approximated by small discrete cubes (voxel) that can easily be used for volume calculation. Since the clusters are composed of non-intersecting pebbles and each pebble is considered as a separate solid, the volume calculation leads to the same result as in the first approach. The voxelization approach is only useful for clumps with intersecting pebbles in order to prevent that overlaps are counted twice. Therefore, only the first approach was used for volume calculation.

Clusters represent a set of bonded spheres that can break under mechanical loading when the stress exceeds the local contact strength. When a cluster splits into two parts, the resulting fragments must be registered as separate clusters. The newly built-in fragment logic (PFC3D 5.0) was used for that purpose which automatically computes fragments at given time-intervals during simulation. Fig. 3.17 shows the cluster sample with increasing compaction.

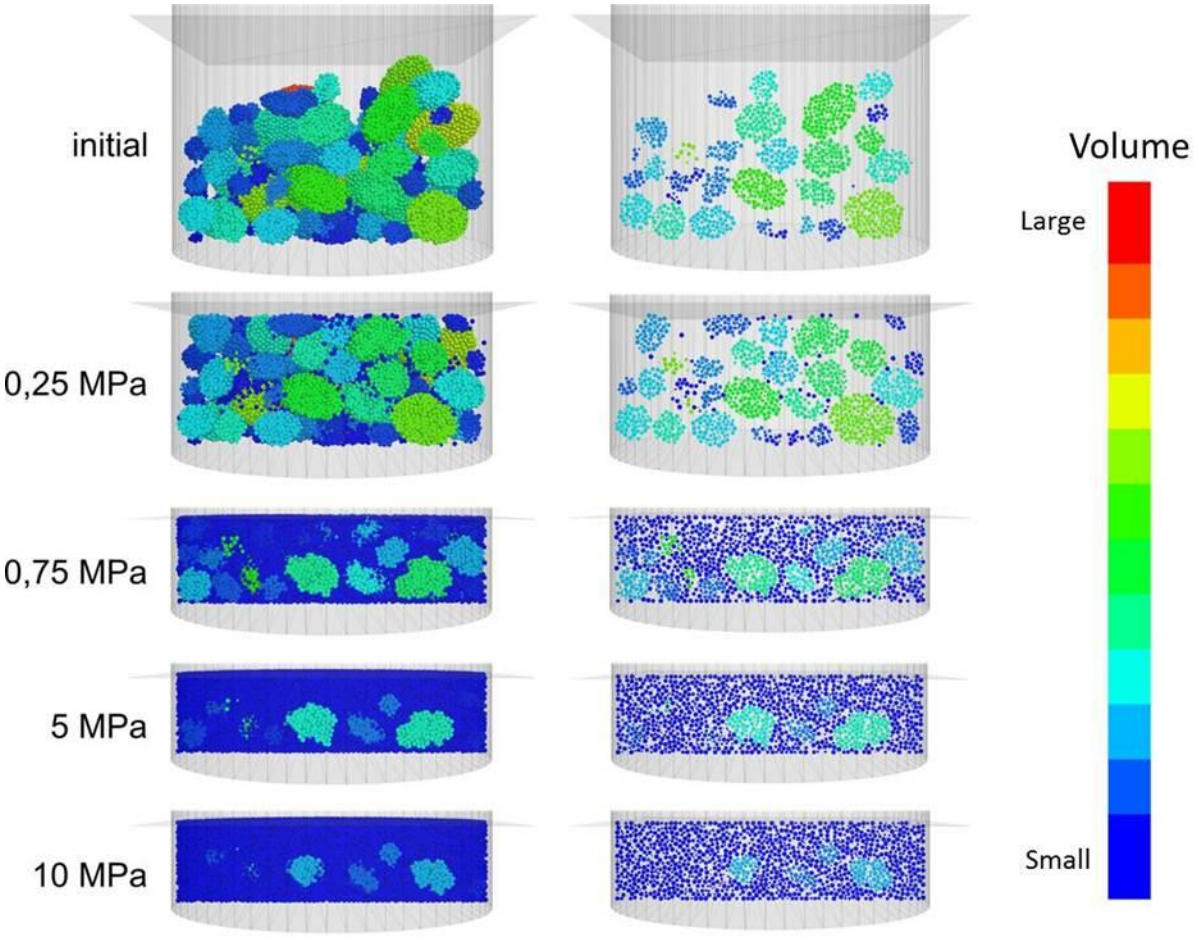

Fig. 3.17: Compaction of the clusters for different stress levels. A vertical cutting plane was used in order to show in a) a half-cylinder and in b) a thin-section.

When loading starts, the compaction is mainly characterized by a rearrangement of grains. However, plastic deformation in terms of grain crushing starts relatively early at stress levels of 0.5 MPa. Grain crushing was mostly observed for single spheres at the outer shell of a cluster. Due to fewer contacts to the cluster, these spheres can be disconnected more easily. The separation of single spheres leads to the fact that larger particles became progressively

smaller with increasing stress. At an applied stress of 0.75 MPa for example the sample still consists of clusters but they are surrounded by an increased amount of single spheres.

Fig. 3.18 shows the porosity and strain versus stress. When loading starts, the rearrangement of clusters leads to a large reduction in porosity. The porosity reveals an axial strain accumulation of over 70% and a reduction in porosity to 45% at 1 MPa loading stress for the cluster model (Fig. 3.18 left). With increasing axial stress, the strain rate is decreased and the porosity is reduced only slightly to a value of 42%. The evaluation of the clump model reveals a quite similar behavior during the mechanical loading (Fig. 3.19).

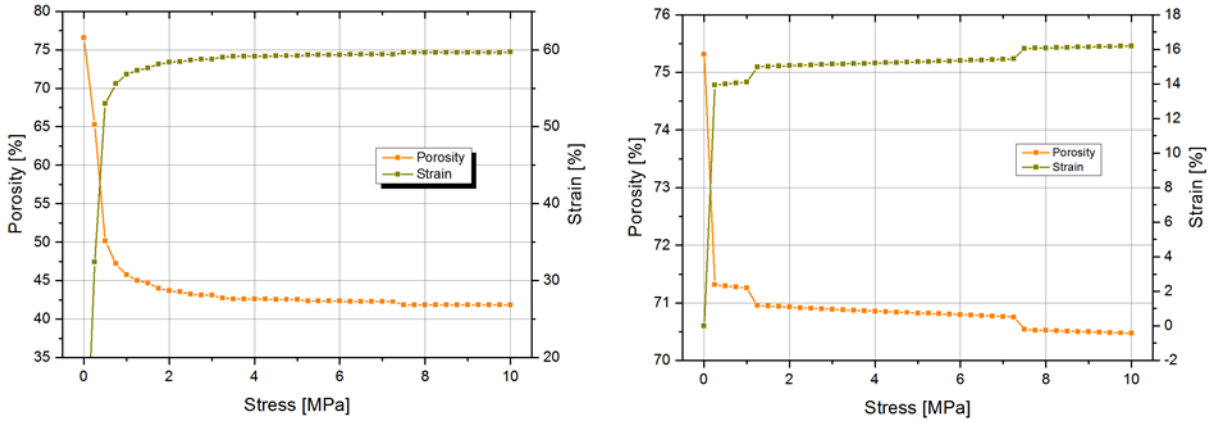

Fig. 3.18: Calculated porosity and strain versus axial stress of the cluster model (left) and the clump model (right).

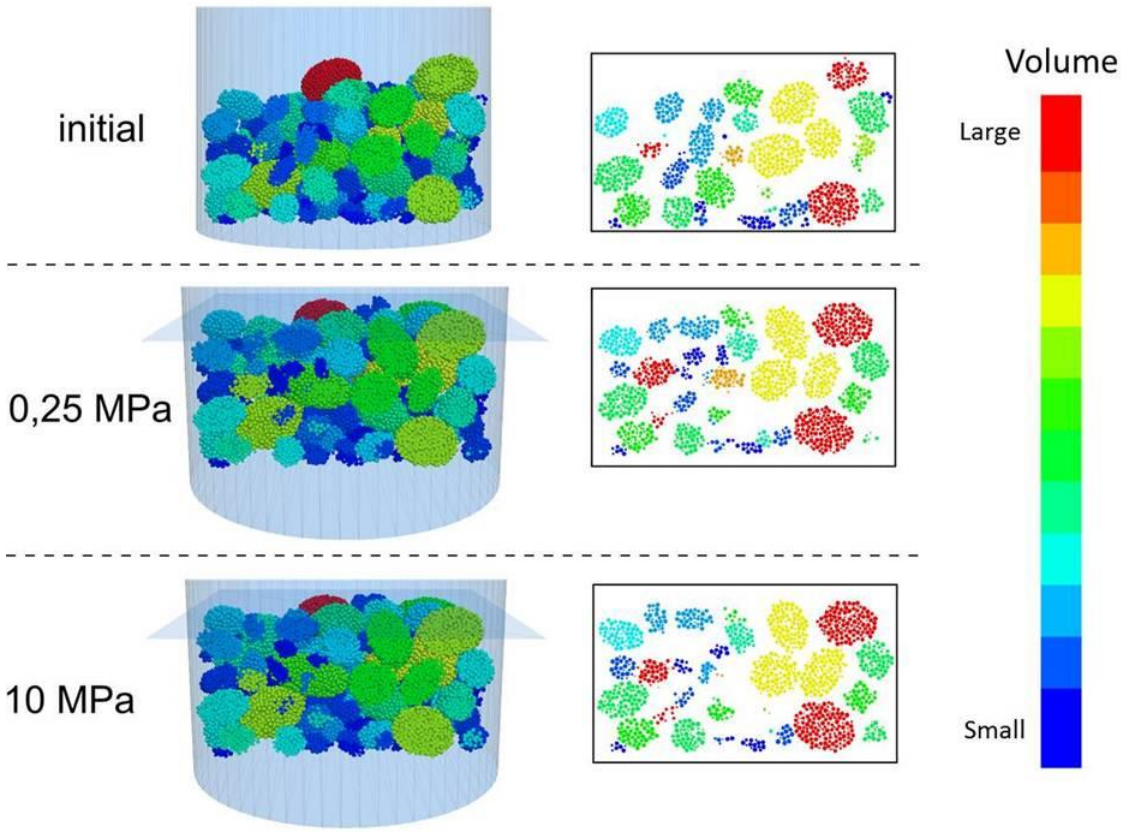

Fig. 3.19: Compaction of the clumps for different stress levels. A vertical cutting plane was used in order to show in a) a half-cylinder and in b) a thin-section.

The deformation of the sample is mainly due to rearrangement of clumps leading to an abrupt reduction in porosity (Fig. 3.18 right). However, since clumps represent rigid bodies that cannot break with increasing stress, a further deformation is limited due to interlocking effects between the larger clumps.

As mentioned above the calculated porosity of the PFC models are too high due to the pore space between the pebbles within each individual cluster or clump which is included in the calculated porosity value but cannot be separately determined and thus subtracted. To get at least an idea of the porosity reduction due to compaction, the calculated porosity has been normalized to its maximum value at the initial stage. This allows for an estimation of the percentage decrease in pore space during mechanical loading. This normalized or relative porosity is plotted in (Fig. 3.20). As can be seen the cluster model yields a porosity reduction of about 45% whereas the clump model yield a reduction of less than 10% only.

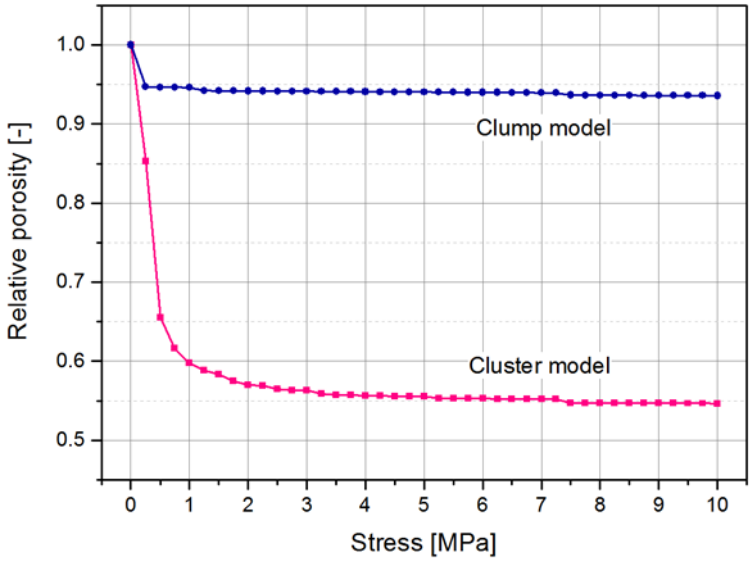

Fig. 3.20: Relative (normalized) porosity versus axial stress for both, the cluster and the clump model.

3.6.2 The 3DEC Model

In order to generate a very similar particle sample for 3DEC, the PFC3D particle model (after settling) was converted to a corresponding 3DEC volume elements model using the methods already described in chapter 3.4.2. Since the surfaces of the volumes are based on the convex hull algorithm that uses the center coordinates of the spheres, the method leads to slightly smaller volumes in case they do not touch each other. Therefore, some calculation runs must be performed first to make sure that the particles are in mechanical equilibrium. The following procedure is the same as for the PFC3D Model. A loading plate was generated and provided with a velocity boundary condition to compact the sample using a force of 10 MPa. Furthermore, the velocity was adjusted in order to avoid that the sample is not loaded faster than the stresses can be transferred numerically through the sample. The internal programming language FISH was used to record the stresses, the strain and the porosity of the sample at certain intervals. However, due to numerical problems with regard to contact detection and in contrast to the initial intention only 3DEC models with non-deformable polyhedral elements could be investigated.

Fig. 3.21 shows the 3DEC model at different compaction levels. After start of the mechanical loading, the compaction is characterized by a rearrangement of grains (blocks).

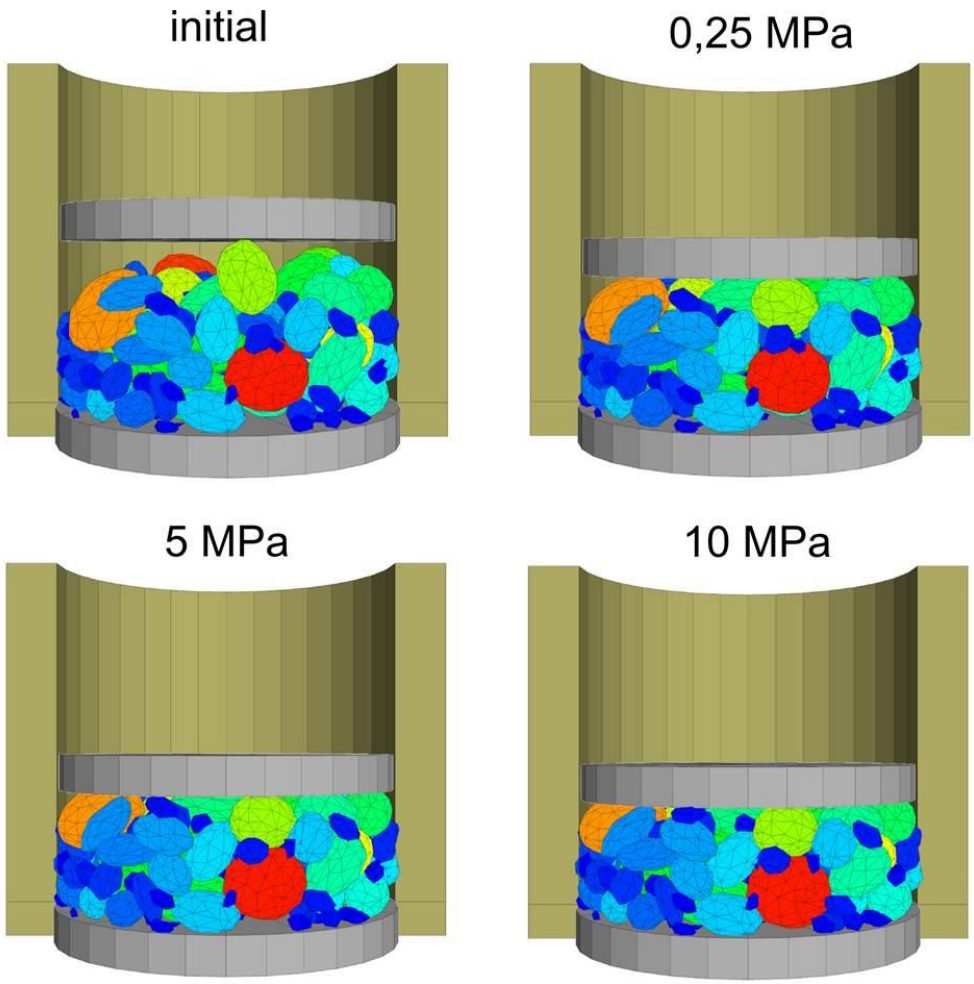

Fig. 3.21: Compaction status of the polyhedral elements at different stress levels

Since the polyhedral elements represent rigid bodies, interlocking effects arise very quickly. As a consequence, the compaction to axial stresses of about 10 MPa is achieved without visually significant rearrangement of grains. Mechanically the interaction between two contacting polyhedral elements is described by stiffness springs in the normal and shear direction. Depending on the contact stiffness, this includes a certain amount of contact overlap. Therefore, with increasing stress a considerable part of the strain is mainly caused by interpenetration of adjacent blocks. The porosity of the model is reduced from 61 % to 41 % (Fig. 3.22) which corresponds to a reduction of about 34%.

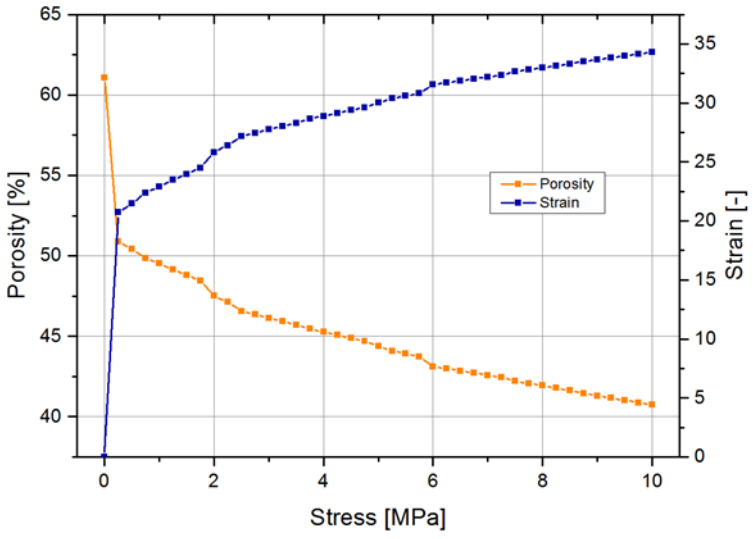

Fig. 3.22:
Calculated porosity and strain versus axial stress for the 3DEC model.

3.7 Discussion

The objective of the work was to test the suitability of the discrete element method (DEM) for modelling the compaction of granular salt. The advantage compared to the commonly used continuum approach is the explicit consideration of particles. It is thus possible to study the fracture and damage behavior of a granular media at grain scale. Two different approaches, the PFC3D and the 3DEC code from Itasca, were investigated. The PFC3D uses not deformable spheres as the basic elements which were grouped to so-called clumps (rigid set of spheres) and clusters (deformable set of spheres) in order to represent the particle shape of granular rock salt. The deformability of a particle arrangement is realized solely through contacts between the spheres. The 3DEC model consists of arbitrarily shaped blocks that can be rigid or deformed due to continuum mechanical approaches.

A detailed description of the material is a very important aspect, since the grain size distribution and the particular grain shape significantly affect the compaction behavior of granular rock salt. The DEOPARA grain-size curve was used and, in addition, computerized particle analyzer (CPA) measurements were carried out to characterize the grain-shape. When generating the grains some simplifications had to be made due to code-specific functionalities. To avoid the generation of very small particles, the grain-size distribution was limited to particles greater than 1.5 mm using a cut-off condition. Furthermore, the particles are described as ellipsoids for better handling using the length-width ratio of the CPA analysis. The CPA analyses show, however, that the particles may be considered as relative angular. The influence of angularity on the compaction behavior was not investigated.

A significant drawback of the DEM method is that material parameters used in the constitutive models are difficult to obtain from classical laboratory experiments. The identification of material parameters is oftentimes conducted by back-calculation of laboratory experiments. However, it turned out that this kind of calibration procedure with samples containing many particles is too time consuming. This applies in particular to the use of PFC3D. Therefore, an attempt was made to calibrate the individual PFC3D cluster particles so that their mechanical behavior corresponds to a salt grain. Since laboratory tests on single crushed salt particles are not available, the assumption was made that the mechanical behavior of a single salt crystal is the same as a consolidated rock salt sample. Furthermore the assumption was made that all clusters have the same strength values because size-dependent or shape-dependent values are not available.

Further development is needed with respect to the material models used, particularly in PFC3D. A stiffness model and a bonding model were used in PFC3D in order to simulate the elasto-plastic deformation behavior. The impact of time-dependent creep on the mechanical behavior was not incorporated in this simulation. PFC3D supplies built-in constitutive models for simulating creep (simple viscoelastic model, Burger's model). However these models are not suitable for modelling the compaction of granular rock salt since creep inside clusters does not work. More advanced constitutive models for PFC3D are under development. 3DEC, however, is based on continuum mechanical approaches where appropriate models for simulating the deformation of rock salt exist. Due to numerical problems with regard to contact detection and the extreme long calculation times only rigid blocks were analyzed

though. It should be noted, that 3DEC was initially developed for simulating the mechanical behavior of larger jointed rock masses rather than simulating granular flow.

One disadvantage of the DEM method appears when modelling the oedometer tests. Due to long numerical calculation times when using the usual laboratory sample geometry, the compaction tests had to be carried out on samples with significantly reduced diameter. Using the REV concept, this leads to a sample dimension that is far below the smallest volume that is necessary for measurements. Generally, the diameter of the sample should be ten times the largest grain size in the sample. Since the particles are rather large in relation to the cylindrical container, interlocking effects arise relatively quickly between the larger particles when loading starts. A further rearrangement of grains is suppressed and peak stresses are generated leading to an unrealistic fracture behavior of the clusters by losing more and more single spheres at the outer shell of a cluster. At the time being, necessary calculation times for the compaction of particle arrangements representing real oedometer conditions is far beyond practical application.

A further difficulty arises for the analysis of porosity especially in PFC3D. The calculated porosity of the PFC models are too high due to the pore space between the pebbles within each individual cluster or clump which is included in the calculated porosity value but cannot be separately determined and thus subtracted. In 3DEC the volume of the blocks can be explicitly determined. However, the code specific method used to describe the interaction of blocks leads to an interpenetration of adjacent blocks. This causes undefined errors when calculating the porosity, which cannot be corrected.

3.8 Statistical structure analysis

As described in the previous chapter the determination of the porosity of the model during compaction and thus at different compaction states is difficult in PFC. Different tools have recently been implemented which may deliver additional information about the particle and pore structure of the model domain (Wagner & Konietzky, 2013). These tools and their outcomes with regard to the PFC3D compaction model are described in the following subsections.

3.8.1 Contact distribution

Contact distributions characterize in some way the size and shape of the pore space inside a packing of hard spheres. The main types are the linear and spherical contact distributions (Wagner et al., 2010). The linear contact distribution characterizes the linear extent of the pores. It is a probability density function of a randomly length and is calculated as the distance between a randomly chosen point in the pore space and the first contact with a sphere in a prescribed (or random) direction (Fig. 3.23).

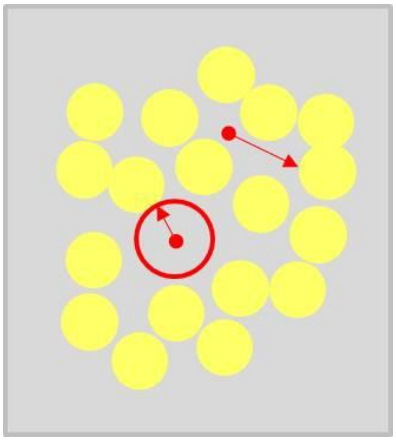

Fig. 3.23:
Principle of linear and spherical contact distribution determination.

The spherical contact distribution is a generalization of the linear contact distribution function. The difference is, that not a given direction has to be chosen but a sphere around the random point in the pore space is blown up until the first contact with the surface of a sphere occurs. Some more details are given in Wagner et al. (2010) and Stoyan et al. (2011).

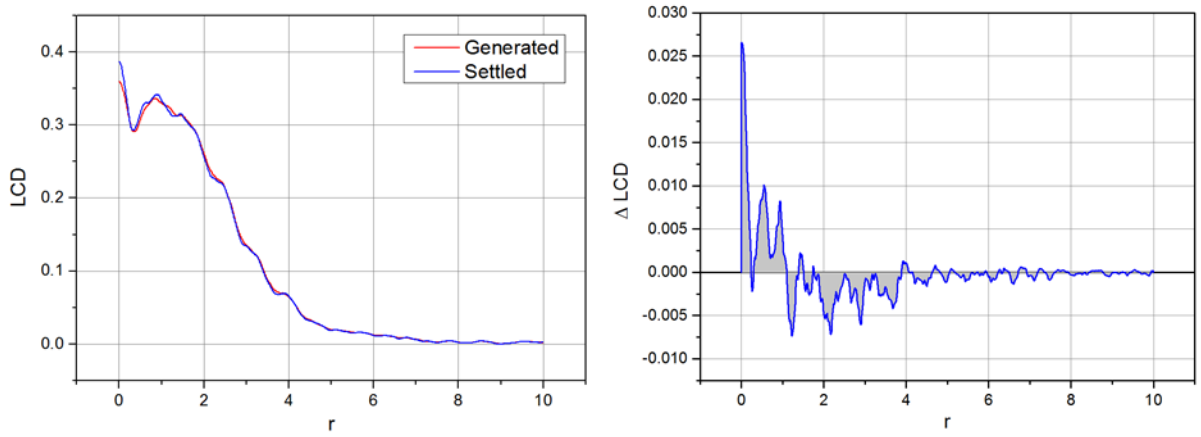

Fig. 3.24: Linear contact distribution of the particle arrangements described for the oedometer test model in chapter 3.6.1 after particle generation and after gravitational settlement.

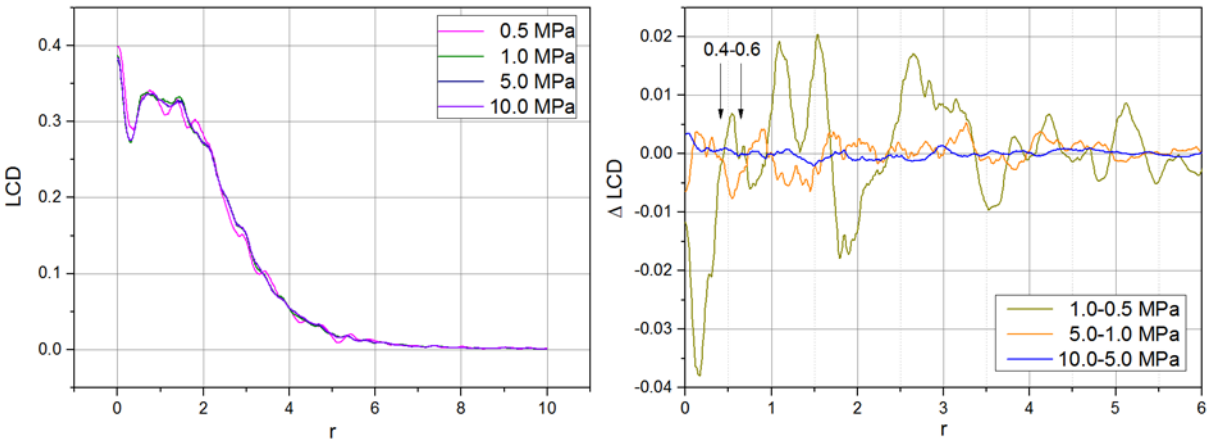

Fig. 3.25: Linear contact distribution of the particle arrangements described for the oedometer test model in chapter 3.6.1 after different mechanical loading steps.

Fig. 3.24 (left) shows the linear contact distribution of the particle arrangements described for the oedometer test model in chapter 3.6.1 after particle generation and after gravitational settlement. It says for example that out of N tests the probability to obtain a length of 2 is about 25%. Since the change in the absolute values is rather small it is better to look at the differences. The image on the right shows the difference of both curves. It is obvious that the probability to detect pore spaces in the distance range from 1 to 4 is significantly reduced after settlement whereas the probability to detect pore spaces in the range of 0 to 1 is significantly increased.

The results of the following mechanical loading steps are plotted in Fig. 3.25 for both the linear contact distributions (left) and the difference curves (right). In the left figure it can be seen that the probability to get a length between about 0.5 and 1.5 is more or less constant for all loading steps. This is a first indication that the possibility of compaction is limited. In the right

figure one can see that during the 1 MPa loading step (green curve) the pore lengths in the range of 0 to 0.4 are significantly reduced (negative peak). In the same curve in the range of 1.0 to 1.6 higher pore space densities are generated due to the elimination of larger pores in the range of 1.6 to 2.0. Looking at the orange and the green curve, it can be observed that both curves show opposing trends in the distance range from 0 to 4. For example in the range of 0.4 to 0.6 pore spaces are generated during the 1 MPa phase which are completely eliminated during the following 5 MPa loading step. That means in this particular pore space range there is no compaction. This confirms the result of the K-function and the paircorrelation function, described in the following sub-chapters, for this range (Fig. 3.28 right and Fig. 3.29 right) which indicates no compaction as well.

In Fig. 3.26 the spherical contact distribution (blue curve) is plotted versus the linear contact distribution (red curve). The load step of 0.5 MPa was chosen as an example. In principle the figure is tripartite. For small pore spaces in the range of 0-1.2 the probability to find more spherically shaped pore volumes is much higher than to detect longish pore volumes. In the second range from 1.2 to 4.2 the probability to find spherically shaped pore volumes decreases significantly. In this area the more longish pore spaces prevail considerably. Larger pore spaces are rare and the probability to detect them is almost zero for both the spherically shaped and the longish ones.

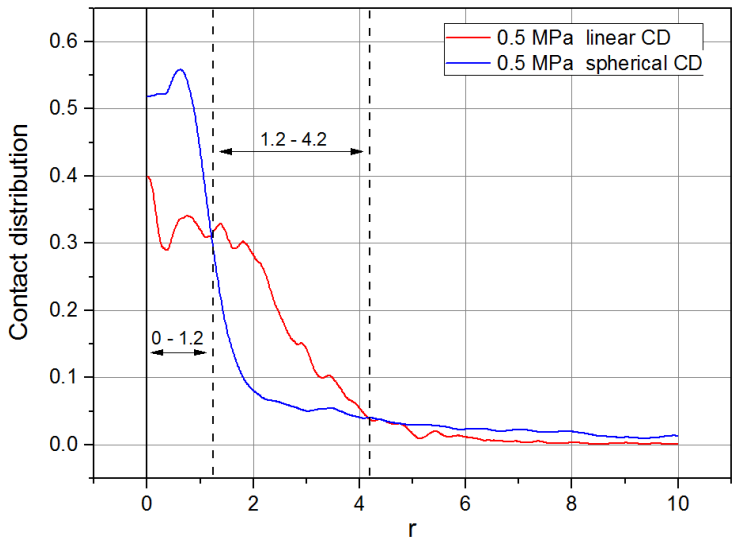

Fig. 3.26:
Comparison of the linear and the spherical contact distribution.

3.8.2 Paircorrelation function

The paircorrelation function g(r) characterizes a local sphere arrangement. It gives the frequency of distances between the sphere centres. In practice, different spheres are randomly chosen and the distances of their centres to the centres of neighbouring spheres are determined. Building mean values over a couple of determinations and normalizing them to the mean particle density yields the paircorrelation function of the particle arrangement.

In Fig. 3.27 the relation between structure and particle number density is illustrated. This sketch shows that the first maximum is produced by the nearest neighbouring spheres which usually appears at a distance which is approximately the mean diameter of the spheres. The next maximum is produced by the following particle shell and so on. With increasing distance the maxima are getting more and more smeared due to the missing long-range order and thus less characteristic. Due to the normalization, at large distances the paircorrelation function approaches 1.

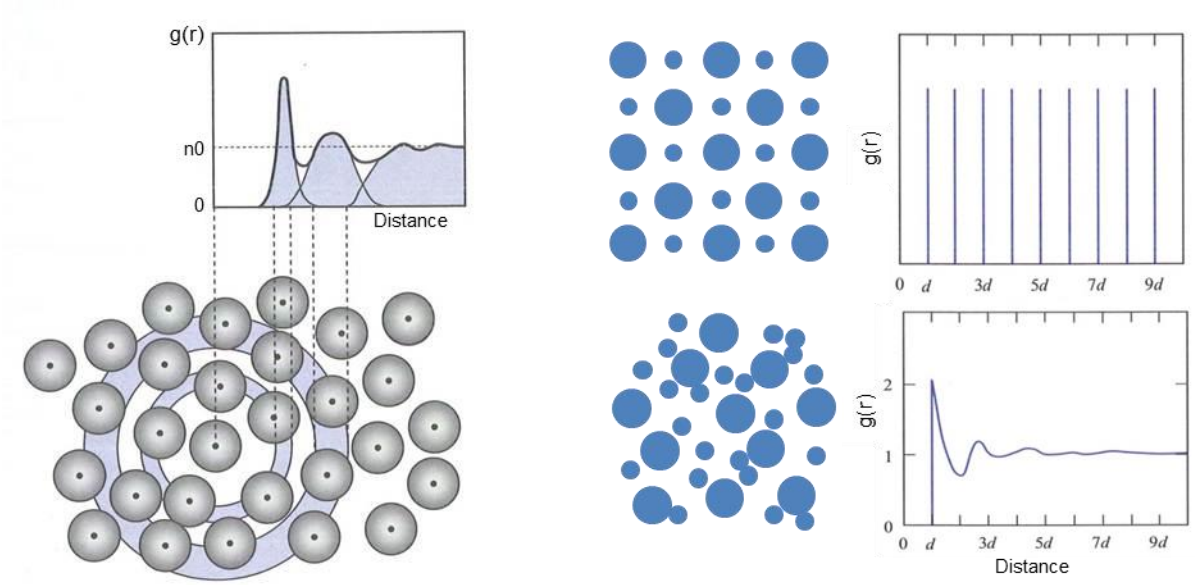

Fig. 3.27: (left) Illustration of the relation between structure and particle number density; (right): principle appearance of the paircorrelation function for crystalline structures (upper part) and amorphous structures (lower part). Images modified after Hunklinger (2011).

In crystalline systems e.g. peaks occur in the paircorrelation function at the typical distances of the atomic grid (Fig. 3.27, upper left image). In this case the peaks occur in form of a delta function. Within amorphous structures the peaks are less discrete and much more smeared-out (Fig. 3.27 lower left image).

Fig. 3.28 shows the paircorrelation function of the particle model of the oedometer test (left) together with the difference curves of two consecutive load steps (right). The shape of the curves clearly indicates that the sphere structure shows an amorphous character. All curves in the left image have a peak at r = 0.4 which is the diameter of the spheres (r/d=1). That means that this peak belongs to pairs of spheres with direct contact. The next maximum is a broad one in the distance range of about 0.6 to 0.8. The latter distance represents a radius to diameter ration of r/d=2 which belongs to a chain of three spheres. The fact that there is a broad maximum between 0.6 and 0.8 indicates that there are a lot of spheres with a distance of less than its diameter. That means there is not enough space for another sphere in-between and that it represents a pore volume. This is also valid for the maxima around r=1.4 and r=1.6. The fact that there is no maximum at r=1.2 (r/d=3) means that there is no strait line of three spheres which is another indication of an amorphous structure.

Looking at the difference curves (Fig. 3.28 right) it can be seen that for the last two loading steps all maxima disappeared except a very small one at r between 0.4 and 0.5. The disappearance of the maxima indicates that there is no more change of the structure in its core during the last two loading steps. Fix cluster structures have been build which are not divided anymore at larger pressures. The only remaining changes are related to distances of r<0.5 indicating that only very small pore volumes are still compacted whereas larger pore spaces are kept between the sphere clusters and thus not compacted anymore.

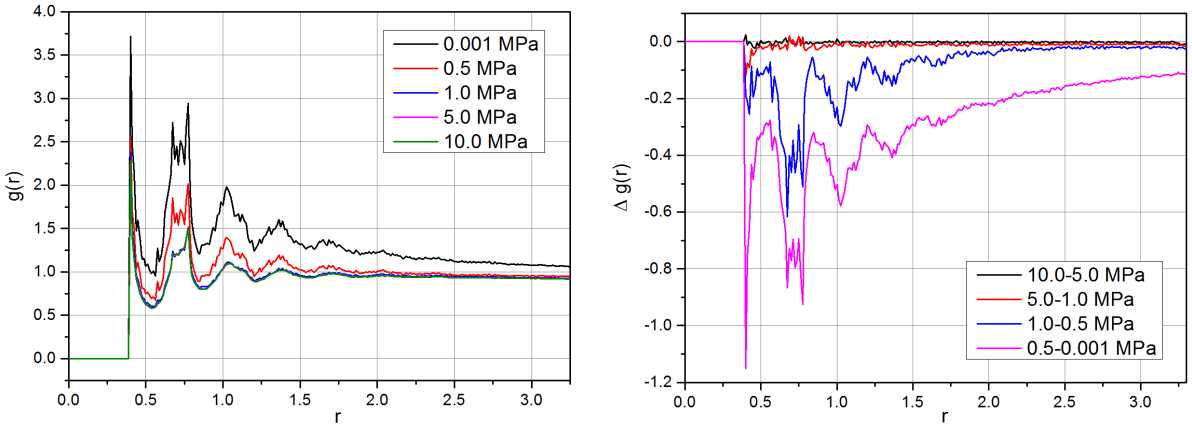

Fig. 3.28: Paircorrelation function of the particle model of the oedometer test (left) together with the difference curves of two consecutive load steps (right).

3.8.3 Ripley's function

The Ripley's K-function is a spatial analysis method used to describe how point patterns occur over a given area of interest. It is an integrated paircorrelation function and it counts the sphere centres lying within a growing sphere with radius r around one of the sphere centres of a sphere packing. Thus the K-function gives the average number of sphere centres in the range of r of another sphere centre (Wagner et al., 2010; Wagner & Konietzky, 2013). The K-function allows determining if the phenomenon of interest appears to be dispersed, clustered, or randomly distributed throughout the study area. Ripley's K-function is generally calculated at multiple distances allowing to see how point patterns (particles) distributions can change with scale. For example, at near distances, the particles could cluster, while at farther distances, particles could be dispersed. More information about the K-function can be obtained from Dixon (2002) and Kiskowski (2009).

For our simple particle model with mono-dispersed spheres consisting of the same material, the outcome is limited. In the case of the model described in chapter 3.6.1 the result is: the steeper the curve the greater the density of the model. The K-functions for the different states of compaction are plotted in Fig. 3.29 (left). The curves start to deviate from zero at about 0.4 cm which is the diameter of the spheres in the model. This graph clearly indicates that the compaction process more or less stops at the 5 MPa stage.

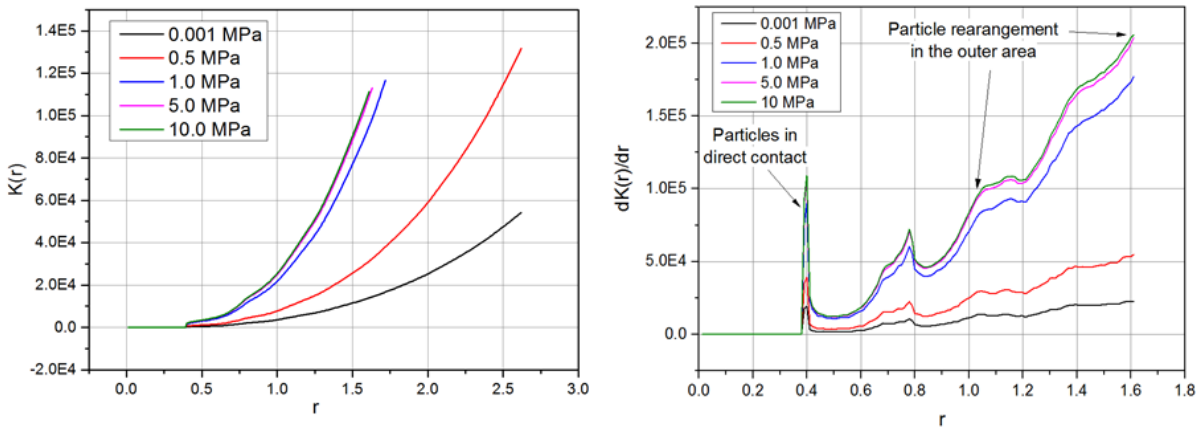

Fig. 3.29: K-functions and their first derivatives of the five different compaction states of the model.

Even doubling the compacting force from 5 MPa to 10 MPa yields no more significant compaction.

By looking at the first derivatives of the K-functions (Fig. 3.29, right) the following remarks can be made: The peak at 0.4 (sphere diameter) indicates particles with direct contact. The higher the mechanical load the more direct contacts appear. In the distance range between 0.4 and 0.6 a significant compaction only occurs during the load step of 1.0 MPa. The compaction during the prior step is very small and for higher load steps almost zero indicating that a possible rearrangement of particles in that range is not accompanied by a reduction in distances of the spheres. At a distance of about 1.0 the curves for 5 and 10 MPa start to diverge slightly. This indicates that during the last load step additional (slight) compaction occurs mainly in the outer area of the model and not in the core any more.

4 Conclusions and outlook

The thin section analyses show that the higher the compaction of a sample the more are the remaining pathways, which could be penetrated by the raisin, located at the boundaries of larger grains. The addition of 1.2% salt solution during compaction obviously had the effect that the small grains in the fine grained section “bonded’’ leading to new crystalline structures so that the amount of fine pores in this section was reduced significantly. By contrast, the addition of moist air during compaction did not lead to such bonding. The sample that had been permeated with brine after dry compaction shows a lot of very local penetrated areas (hot spots). This indicates that leaching took place during permeation, which led to the formation of a “vessel system” that could be permeated by the resin. This vessel system seems to be permanent. With regard to the real situation in a repository where crushed salt is used as backfill material in the drifts, this could indicate that the occurrence of an early brine pressure in the crushed salt; i.e. when it has not yet completely compacted, could lead to the formation of an unwanted system of larger pores which might remain for a certain period of time until it is compacted and closed by the convergence.

So far, there are no systematic studies that deal with the simulation of the compaction of granular rock salt at grain scale using the discrete element method. To test their suitability for modeling the compaction of granular rock salt the DEM was used as an exploratory analysis. Two different computer codes have been used for this analysis, the PFC3D and the 3DEC code. During the application analysis a couple of problem occurred with both of the codes which are, amongst others, related to porosity determination and most of all related to necessary calculation times that are far beyond practical application. Further development is needed with respect to the material models used, particularly in PFC3D. The impact of time-dependent creep on the mechanical behavior could not be incorporated in the simulations. 3DEC, however, is based on continuum mechanical approaches where appropriate models for simulating the deformation of rock salt exist. But significant numerical problems occurred mainly with regard to particle contact detection. Finally, it has to be stated that both codes need significant improvements prior to an application to simulate compaction processes.

A computer tomographic analysis with XCT and FIB-nt has been applied to samples which differ substantially in porosity. The analysis reveals that the pore space must be considered as isotropic in its connectivity and percolation threshold. Micropores with radii <1 µm can often be observed along grain boundaries of otherwise compact salt grain aggregates. Often the pore geometry is defined by crystallographic planes, which suggest that these pores are related to the formation of fluid inclusions which are per se not connected. By applying an approach, which combines local porosity theory and percolation theory, to reconstructed pore structures, gives an idea of the critical porosity (percolation threshold). From the investigation of these samples it can be stated that, on the one hand for porosities exceeding 5% a fully connected and thus percolating pore network must be taken into consideration. On the other hand for porosities of 1% or less the pore network can be assumed as very poorly or even not connected.

5 References

Baumgarten, l., & Konietzky, H. (August 2010). Investigations in the fracture behaviour of rocks in a triaxial compression test. In D. V. für Materialforschung und.prüfung e.V. (Hrsg.), Fracture of Materials and Structures from Micro to Macro Scale; Proc. European Conference on Fracture (ECF-18), Dresden, (S. 1-9).

Bechthold, W., Smailos, S., Heusermann, S., Bollingerfehr, W., Bazargan Sabet, B., Rothfuchs, T., et al. (2004). Backfilling and Sealing of Underground Repositories for Radioactive Waste in Salt (BAMBUS II Project), Final Report. Tech. rep., European Commission, EUR 20621 EN.

BMU. (2010). Sicherheitsanforderungen an die Endlagerung wärmeentwickelnder radioaktiver Abfälle. Sicherheitsanforderungen an die Endlagerung wärmeentwickelnder radioaktiver Abfälle.

Bunde, A., & Havlin, S. (1995). Percolation I, Fractals and Disordered Systems. (A. Bunde, & S. Havlin, Hrsg.) Berlin: Springer.

Cinar, Y., Pusch, G., & Reitenbach, V. (2006). Petrophysical and Capillary Properties of Compacted Salt. Transport in Porous Media, 64, 199-228.

Cleary, P. W. (2004). Large scale industrial DEM modelling. Engineering Computations, 21(2/3/4), 169-204.

Cundall, P. A. (1980). UDEC-A Generalised Distinct Element Program for Modelling Jointed Rock. Tech. rep., DTIC Document.

D'Addetta, G. A. (2004). Discrete Models for Cohesive Frictional Materials. Ph.D. dissertation, Universität Stuttgart.

Dixon, P. (2002). Ripley's K-function. In A. H. El-Shaarawi, & W. W. Piegorsch (Hrsg.), Encyclopedia of Environmetrics (S. 1796-1803). John Wiley \& Sons, Ltd, Chichester.

Dong, H., & Blunt, M. (2009). Pore-network extraction from micro-computerized-tomography images. Physical Review, E80(036307).

Groh, U., Konietzky, H., Walter, K., & Herbst, M. (2011). Damage simulation of brittle heterogeneous materials at the grain size level. Theoretical and Applied Fracture Mechanics, 55(1), 31-38.

Heemann, U., Sarfeld, W., & Faust, B. (2010). THMC- Enwicklung von Methoden zur interaktiven Simulation gekoppelter thermischer, mechanischer, hydraulischer und chemischer Prozesse : Statusbericht 2010 zum Entwicklungsstand des FE-Programms JIFE. Statusbericht, BGR, Hannover.

Hein, H. (1991). Ein Stoffgesetz zur Beschreibung des thermo-mechanischen Verhaltens von Steinsalzgranulat. Master's thesis, RWTH Aachen.

Hilfer, R. (2000). Local porosity theory and stochastic reconstruction for porous media. In: LNP 554, Eds.: K.R. Mecke and D. Stoyan, pp. 203-241, 2000, Springer-Verlag Berlin Heidelberg.

Hu, J. & Stroeven, P. (2004). Local porosity analysis of pore structure in cement paste. Cement and Concrete Research 35, pp. 233-242, 2004, Elsevier, (doi:10.1016/j.cemconres.2004.06.018).

Hunklinger. (2011). Festkörperphysik (Third edition Ausg.). Oldenbourg Verlag.

Hunsche, U., & Schulze, O. (2001). Humidity induced creep and it‘s relation to the dilatancy boundary. Basic and Applied Salt Mechanics - Proc. of the Fifth Conf. on the Mech. Behavior of Salt, Bucharest 1999.

Itasca. (2003). PFC3D Manual – Theory and Background.

Itasca. (2013). 3DEC - 3 Dimensional Distinct Element Code Users's Guide.

Jing, L. (2003). A review of techniques, advances and outstanding issues in numerical modelling for rock mechanics and rock engineering. International Journal of Rock Mechanics and Mining Sciences, 40(3), 283-353.

Kanit, T., Forest, S., Galliet, I., Mounoury, V., & Jeulin, D. (2003). Determination of the size of representative volume element for random composites: statistical and numerical approach. Int. Jour. of Solids and Structures, 40, 3647-3679.

Kazerani, T., & Zhao, J. (2010). Micromechanical parameters in bonded particle method for modelling of brittle material failure. International journal for numerical and analytical methods in geomechanics, 34(18), 1877-1895.

Keller, L., Holzer, L., Schuetz, P., & Gasser, P. (2013). Pore space relevant for gas permeability in Opalinus clay: Statistical analysis of homogeneity, percolation, and representative volume element. Journal of Geophysical Research: Solid Earth, 118(doi: 10.1002/jgrb.50228), 1-14.

Kenobi, O.W. (1999). Star Wars, The Phantom Menace, Lucasfilm Ltd, USA

Kiskowski, M., Hancock, J., & Kenworthy, A. (2009). On the Use of Ripley's K-Function and Its Derivatives to Analyze Domain Size. Biophysical Journal, 97, 1095-1103.

Kröhn, K.-P., Stührenberg, D., Herklotz, M., Heemann, U., & Lerch, C. X. (2009). Restporosität und -permeabilität von kompaktierendem Salzgrus-Versatz - REPOPERM Phase 1. Tech. rep., Gesellschaft für Anlagen- und Reaktorsicherheit (GRS) mbH - gefördert durch das BMWi 02 E 10477.

Krone, J., Bollingerfehr, W., Filbert, W., Keller, S., Lommerzheim, A., Mönig, J., et al. (2013). Status of the safety concept and safety demonstration fon a HLW repository in salt. Summary Report, DBE TECHNOLOGY GmbH, BGR, GRS.

Lantuejoul, C. (1991). Ergodicity and intergral range. J. Microsc., 161, 387-403.

Liu, J., & Regenauer-Lieb, K. (2011). Application of percolation theory to microtomography of structured media: Percolation threshold, critical exponents, and upscaling. Physical Review E, 83, 016106.

Münch, B., & Holzer, L. (2008). Contradicting geometrical concepts in pore size analysis attained with electron microscopy and mercury intrusion. J. Am. Ceram. Soc., 91, 4059-4067.

Peng, S., Hu, Q., Dultz, S., & Zhang, M. (2012). Using X-ray computed tomography in pore structure characterization for a Berea sandstone: Resolution effect. Journal of Hydrology, 472-473, 254-261.

Popp, T., Salzer, K., Schulze, O., & Stührenberg, D. (05 2012). Diskussionsbeitrag zum Kompaktionsverhalten und den hydraulischen Eigenschaften von Salzgrusversatz. unpublished.

Pringle, D., Miner, J., Eicken, H., & Golden, K. (2009). Pore space percolation in sea ice single crystals. Journal of Geophysical Research, 114, C12017.

Renard, F., Bernard, D., Thibault, X., & Boller, E. (2007). Synchrotron 3D microtomography of halite aggregates during experimental pressure solution creep and evolution of permeability. Geophys. Res. Lett., 31(L07607).

Spangenberg, E., Spangenberg, U., & Heindorf, C. (1998). An experimental study of transport properties of porous rock salt. Physics and Chemistry of the Earth, 23(3), 367-371.

Spiers, C., Grupa, J., Salzer, K., Popp, T., & Stürenberg, D. (2005). Buffer / backfill in salt (long-term compaction, additives, precompacted bricks) - Talk. 2nd NFPRO-Workshop, Cardiff (GB).

Spiers, C., Peach, C., Brzesowsky, R., Schutjens, P., Liezenberg, J., & Zwart, H. (1989). Long-term rheological and transport properties of dry and wet salt rocks. Final report, Commission of the European Communities.

Spies, T., van den Horn, B., Prij, J., Rothfuchs, T., & Müller, K. (1993). Sealing of Haw-Boreholes in Salt Formations (Debora-Project). 3. Progress Meeting PEGASUS, Cologne, June 3-4, 1993.

Stauffer, D., & Aharony, A. (1995). Perkolationstheory: Eine Einfuehrung. VCH, Weinheim, New York, Basel, Cambridge, Tokyo.

Stoyan, D., Wagner, A., Hermann, H., & Elsner, A. (2011). Statistical characterization of the pore space of random systems of hard spheres. Journal of Non-Crystalline Solids, 357, 1508-1515.

Urai, J., & Spiers, C. (May 2007). The effect of grain boundary water on deformation mechanisms and rheology of rocksalt during long-term deformation. In K. L. M. Wallner (Hrsg.), The Mechanical Behavior of Salt – Understanding of THMC Processes in Salt, Proceedings of the 6th Conference on the Mechanical Behavoir of Salt, 'Saltmech6'. Hannover.

Valvatne, P. (2004). Predictive pore-scale modelling of multiphase flow. Thesis, Imperial College London.

Valvatne, P., & Blunt, M. (2004). Predictive pore-scale modeling of two-phase flow in mixed wet media. Water Resour. Res., 40(W07406).

Wadell, H. (1935). Volume, Shape and Roundness of Quartz Particles. Journal of Geology, 43 (3), 250-280.

Wagner, A., & Konietzky, H. (2013). Funktionale Erweiterung der Software GrainGen zum Thema „Strukturanalyse von Partikelmodellen“. Technical Report, Technische Universität Bergakademie Freiberg, Institut für Geotechnik, Professur für Gebirgs- und Felsmechanik/Felsbau, Freiberg.

Wagner, A., Hütter, M., & Stoyan, D. (2010). More on the microstructural characterization of dense particle gels. Journal of the European Ceramic Society, 30, 1237-1243.

Watson, E., & Brennan, J. (1987). Fluids in the lithosphere, 1. Experimentally determined wetting characteristics of CO2-H2O fluids and their implications for fluid transport, host rock physical properties, and fluid inclusion formation. Earth Planet. Sci. Lett, 85, 497-515.

Wieczorek, K., Masik, S., Behlau, J., & Müller, C. (2014). Virtuelles Untertagelabor im Salz. 11. Fachtagung „Digital Engineering zum Planen, Testen und Betreiben technischer Systeme“, 17. IFF-Wissenschaftstage, Magdeburg.

Yoon, J., Jeon, S., Stephansson, O., & Zang, A. (2010). Testing of Clumped Particle Models in Simulation of Laboratory Rock Fractures in Compression. Fracture of Materials and Structures from Micro to Macro Scale; Proc. European Conference on Fracture (ECF-18), Dresden.

Zhang, C., Schmidt, M. W., Staupendahl, G., & Heemann, U. (1993). Entwicklung eines Stoff¬ansatzes zur Beschreibung des Kompaktierungsverhaltens von Salzgrus. Technischer Bericht, Institut für Statik der Technischen Universität Braunschweig und GSF-Institut für Tieflagerung Braunschweig, Braunschweig.

Appendix

Local porosity:

Input format of 3-D Data used for the calculation of local porosity distribution

The segmented images were transferred into binary images, in which the pores were set to white and the remaining area to black. The resulting images are two-dimensional arrays of ones (i.e. white) and zeros (i.e. black). The images were then read into three-dimensional arrays of 0's and 1's, in which the ones indicate the pore space. The voxel arrays were then regularly subdivided into cubic sub-arrays of N*N*N voxels. This operation divides the analyzed volume into a regular cubic grid/lattice, in which each cell *K(x,L)* is located a position *x* and has an edge length *L* that corresponds to a certain number of voxels. Once the image stacks are subdivided into such a grid it is possible to determine quantities (e.g. porosity and connectivity) for each cell *K(x,L)*, which are then used as input for the calculation of the local porosity distribution. For the small data sets available, the use of non-overlapping cells led to poor statistics with strong fluctuations in the results. To overcome this problem we used overlapping cells (see also Biswal et al. 1998).

Local porosity theory

To characterize the heterogeneity of the material and to evaluate the representativeness of tomographic methods in characterizing the pore space we followed the approach outlined in (Hilfer 1991; Biswal et al. 1998; Hu and Stroeven 2005; Hilfer and Helmig 2004). Based on the gridded 3D array (see above), the local porosity $\phi(x,L)$ can then be measured in each cubic cell *K(x,L)* by counting the numbers of pore voxels. The local porosity distribution is then defined as

$$\mu(\phi, L) = \frac{1}{m}\sum_{i=1}^{m} \delta(\phi - \phi(x_i, L)) \qquad \text{(A.1)}$$

where *m* is number of placements of measurement cells and δ*(t)* denotes the delta function (sometimes called the Dirac delta function). The function $\mu(\phi,L)$ is a measure for the probability to find the local porosity ϕ in a cell with side length *L.*

Regarding permeability and material transfer the question whether or not a pore space percolates is fundamental. A cell *K(x,L)* is considered as percolating in *x*-direction if there exists a continuous path along the pores space which connects the two faces perpendicular to the x-direction. This definition is also applied to the other directions. The following formulation is used as an indicator for percolation.

$$\Lambda_\alpha(x, L) = \begin{cases} 1 \text{ if } K(x,L) \text{ percolates in } \alpha \text{ direction} \\ 0 \text{ otherwise} \end{cases} \qquad \text{(A.2)}$$

The meaning of *α*-direction is defined in Table AI. As an example, Λ_3 indicates that a cell can be traversed along in all three directions, while Λ_1 indicates that there exists at least one direction along which the cell is percolating. Λ_0 indicates a blocking cell.

The local percolation probability is then defined by:

$$\lambda_\alpha(\phi, L) = \frac{\sum_{i=1}^{m} \Lambda_\alpha(x_i, L) \cdot \delta(\phi - \phi(x_i, L))}{\sum_{i=1}^{m} \delta(\phi - \phi(x_i, L))} \tag{A.3}$$

where $\lambda_\alpha(\phi,L)$ is the fraction of cells with local porosity ϕ and side length L that allow percolation in α-direction. A pore space is fully connected if $\lambda_3 = 1$. In practice, the Dirac delta function $\delta(t)$ is seen as kind of limit of a sequence of functions having a tall spike at the origin. Different approximating functions can be defined. Here we used the following function

$$\delta(t) = \frac{1}{2\sqrt{\pi\zeta}} e^{-\frac{t^2}{4\zeta}} \tag{A.4}$$

When plotted against t the above function appears as a narrow spike at $t = (\phi - \phi(x,L)) = 0$ and vanishes outside a very narrow range symmetric around $t = 0$. Thus, if a certain locale porosity is found within a cell, the function acts as a kind of an “impulse response function” and in combination with Eq. (A.1) collects the response of local porosities and yields and continuous functions of local porosity density.